Article

SARS-CoV-2 infection and persistence in the human body and brain at autopsy

https://doi.org/10.1038/s41586-022-05542-y

Received: 3 December 2021

Accepted: 8 November 2022

Published online: 14 December 2022

Check for updates

Sydney R. Stein[1,2], Sabrina C. Ramelli[3], Alison Grazioli[4], Joon-Yong Chung[5], Manmeet Singh[6], Claude Kwe Yinda[6], Clayton W. Winkler[7], Junfeng Sun[3], James M. Dickey[1,2], Kris Ylaya[5], Sung Hee Ko[8], Andrew P. Platt[1,2], Peter D. Burbelo[9], Martha Quezado[5], Stefania Pittaluga[5], Madeleine Purcell[10], Vincent J. Munster[6], Frida Belinky[8], Marcos J. Ramos-Benitez[1,2,11], Eli A. Boritz[8], Izabella A. Lach[1,2], Daniel L. Herr[12], Joseph Rabin[13], Kapil K. Saharia[14,15], Ronson J. Madathil[16], Ali Tabatabai[17], Shahabuddin Soherwardi[18], Michael T. McCurdy[17,19], NIH COVID-19 Autopsy Consortium*, Karin E. Peterson[7], Jeffrey I. Cohen[20], Emmie de Wit[6], Kevin M. Vannella[1,2], Stephen M. Hewitt[5], David E. Kleiner[5] & Daniel S. Chertow[1,2]✉

Coronavirus disease 2019 (COVID-19) is known to cause multi-organ dysfunction[1–3] during acute infection with severe acute respiratory syndrome coronavirus 2 (SARS-CoV-2), with some patients experiencing prolonged symptoms, termed post-acute sequelae of SARS-CoV-2 (refs. [4,5]). However, the burden of infection outside the respiratory tract and time to viral clearance are not well characterized, particularly in the brain[3,6–14]. Here we carried out complete autopsies on 44 patients who died with COVID-19, with extensive sampling of the central nervous system in 11 of these patients, to map and quantify the distribution, replication and cell-type specificity of SARS-CoV-2 across the human body, including the brain, from acute infection to more than seven months following symptom onset. We show that SARS-CoV-2 is widely distributed, predominantly among patients who died with severe COVID-19, and that virus replication is present in multiple respiratory and non-respiratory tissues, including the brain, early in infection. Further, we detected persistent SARS-CoV-2 RNA in multiple anatomic sites, including throughout the brain, as late as 230 days following symptom onset in one case. Despite extensive distribution of SARS-CoV-2 RNA throughout the body, we observed little evidence of inflammation or direct viral cytopathology outside the respiratory tract. Our data indicate that in some patients SARS-CoV-2 can cause systemic infection and persist in the body for months.

COVID-19 has respiratory and non-respiratory manifestations[1–3], including multi-organ failure and shock among patients with severe and fatal disease. Some individuals who survive experience post-acute sequelae of SARS-CoV-2, also known as long COVID[4,5]. Although autopsy studies of fatal COVID-19 cases support the ability of SARS-CoV-2 to infect multiple organs[3,7–12], extrapulmonary organs often lack histopathological evidence of virally mediated injury or inflammation[10–14]. The paradox of infection outside the respiratory tract without injury or inflammation raises many pathogen- and host-related questions.

To investigate the cellular tropism, replication competence, persistence and evolution of SARS-CoV-2 in humans, and to look for associated histopathology in infected tissues, we carried out autopsies on 44 COVID-19 cases. Our approach focused on timely, systematic and comprehensive tissue sampling and preservation for complementary

[1]Emerging Pathogens Section, Critical Care Medicine Department, Clinical Center, National Institutes of Health, Bethesda, MD, USA. [2]Laboratory of Immunoregulation, National Institute of Allergy and Infectious Diseases, National Institutes of Health, Bethesda, MD, USA. [3]Critical Care Medicine Department, Clinical Center, National Institutes of Health, Bethesda, MD, USA. [4]Kidney Disease Section, Kidney Diseases Branch, National Institute of Diabetes and Digestive and Kidney Diseases, National Institutes of Health, Bethesda, MD, USA. [5]Laboratory of Pathology, Center for Cancer Research, National Cancer Institute, National Institutes of Health, Bethesda, MD, USA. [6]Laboratory of Virology, Division of Intramural Research, National Institute of Allergy and Infectious Diseases, National Institute of Health, Hamilton, MT, USA. [7]Laboratory of Persistent Viral Diseases, Rocky Mountain Laboratories, National Institute of Allergy and Infectious Diseases, National Institute of Health, Hamilton, MT, USA. [8]Vaccine Research Center, National Institute of Allergy and Infectious Diseases, National Institutes of Health, Bethesda, MD, USA. [9]National Institute of Dental and Craniofacial Research, National Institutes of Health, Bethesda, MD, USA. [10]University of Maryland School of Medicine, Baltimore, MD, USA. [11]Postdoctoral Research Associate Training Program, National Institute of General Medical Sciences, National Institutes of Health, Bethesda, MD, USA. [12]R Adams Cowley Shock Trauma Center, Department of Medicine and Program in Trauma, University of Maryland School of Medicine, Baltimore, MD, USA. [13]R Adams Cowley Shock Trauma Center, Department of Surgery and Program in Trauma, University of Maryland School of Medicine, Baltimore, MD, USA. [14]Department of Medicine, Division of Infectious Disease, University of Maryland School of Medicine, Baltimore, MD, USA. [15]Institute of Human Virology, University of Maryland School of Medicine, Baltimore, MD, USA. [16]Department of Surgery, Division of Cardiac Surgery, University of Maryland School of Medicine, Baltimore, MD, USA. [17]Department of Medicine, Division of Pulmonary and Critical Care Medicine, University of Maryland School of Medicine, Baltimore, MD, USA. [18]Hospitalist Department, TidalHealth Peninsula Regional, Salisbury, MD, USA. [19]Division of Critical Care Medicine, Department of Medicine, University of Maryland St. Joseph Medical Center, Towson, MD, USA. [20]Medical Virology Section, Laboratory of Infectious Diseases, National Institute of Allergy and Infectious Diseases, National Institutes of Health, Bethesda, MD, USA. *A list of authors and their affiliations appears at the end of the paper. ✉e-mail: chertowd@cc.nih.gov

analyses. We carried out droplet digital polymerase chain reaction (ddPCR) for detection and quantification of SARS-CoV-2 nucleocapsid (N) gene targets and in situ hybridization (ISH) to validate the ddPCR findings and determine the cellular tropism of SARS-CoV-2. Immunofluorescence (IF) and chromogenic immunohistochemistry (IHC) were used to further validate the presence of SARS-CoV-2 in the brain. We carried out quantitative real-time PCR with reverse transcription (RT–qPCR) to detect subgenomic RNA, a marker suggestive of recent virus replication[15], and demonstrated replication-competent SARS-CoV-2 in selected respiratory and non-respiratory tissues, including the brain, by virus isolation in traditional and modified Vero E6 cell culture. In six individuals, we measured the diversity and anatomic distribution of intra-individual SARS-CoV-2 spike gene variants using high-throughput, single-genome amplification and sequencing (HT-SGS).

We categorized autopsy cases as early (n = 17), mid (n = 13) or late (n = 14) by illness day (d) at the time of death, being ≤d14, d15–30 or ≥d31, respectively. We defined persistence as the presence of SARS-CoV-2 RNA among late cases. We analysed and described our results in terms of respiratory and non-respiratory tissues to quantify and statistically compare SARS-CoV-2 RNA levels across tissues and cases.

Autopsy cohort overview

Between 26 April 2020 and 2 March 2021, we carried out 44 autopsies, all among unvaccinated individuals who had died with COVID-19. SARS-CoV-2 PCR positivity was confirmed premortem in 42 cases and postmortem in 2 cases (P3 and P17; Extended Data Fig. 1). A total of 38 cases were SARS-CoV-2 seropositive (Supplementary Data 1a), 3 were seronegative (P27, P36 and P37), and plasma was unavailable for 3 cases (P3, P4 and P15). Brain sampling was accomplished in 11 cases (Fig. 1). The cohort was racially and ethnically diverse. Thirty per cent were female, and the median age was 62.5 years (interquartile range (IQR): 47.3–71.0; Extended Data Table 1a). A total of 61.4% had three or more comorbidities. The median interval from symptom onset to final hospitalization and subsequently death was 6 days (IQR: 3–10) and 18.5 days (IQR: 11.25–37.5), respectively (Extended Data Table 1b). The median postmortem interval was 22.2 h (IQR: 18.2–33.9). Individual-level case data can be found in Supplementary Data 2a.

Widespread infection and persistence

SARS-CoV-2 RNA was detected in 84 distinct anatomical locations and body fluids (Supplementary Data 1b–d), with a significantly (P < 0.0001 for all) higher burden detected in respiratory compared with non-respiratory tissues among early (2.04 ± 0.10 $\log_{10}$[N gene copies] per nanogram of RNA), mid (1.36 ± 0.12 $\log_{10}$[N gene copies] per nanogram of RNA) and late (0.67 ± 0.11 $\log_{10}$[N gene copies] per nanogram of RNA; Extended Data Fig. 2a) cases. We compared linear trends in SARS-CoV-2 RNA levels by illness day, as a continuous variable, and observed a significantly steeper negative slope of SARS-CoV-2 RNA levels in respiratory (−3.14, s.e. 0.39) compared with non-respiratory (−1.62, s.e. 0.38; P < 0.0001) tissues (Extended Data Fig. 2b,c).

We detected SARS-CoV-2 RNA in perimortem plasma of 11 early and 1 mid case (Supplementary Data 1b,d). SARS-CoV-2 RNA was undetectable or just above the limit of detection in peripheral blood mononuclear cells from select early and mid cases (Supplementary Data 1a). The median and IQR of SARS-CoV-2 N gene copies per nanogram of RNA and proportion of cases with RNA detected in each tissue group and fluids are summarized in Extended Data Table 2. SARS-CoV-2 RNA persistence was detected across multiple tissue groups among all late cases despite being undetectable in plasma in any (Supplementary Data 1b–d). SARS-CoV-2 RNA was detected in central nervous system (CNS) tissue in 10/11 cases (90.9%), including across most brain regions evaluated in 5/6 late cases, including P42 who died at D230 (Fig. 1).

We detected SARS-CoV-2 subgenomic RNA across all tissue groups and multiple fluid types, including plasma, pleural fluid and vitreous humour (Supplementary Data 1a–c). ddPCR and subgenomic RNA RT-qPCR results closely correlated among 1,025 jointly tested samples (ρ = 0.76; 95% confidence interval (CI): 0.73–0.78), particularly among respiratory samples (n = 369, ρ = 0.86; 95% CI: 0.84–0.89), early cases (n = 496, ρ = 0.88; 95% CI: 0.85–0.89) and samples that tested positive by both assays (n = 302, ρ = 0.91; 95% CI: 0.88–0.93; Extended Data Fig. 2d,e). With sensitivity and specificity weighted equally, a ddPCR value of ≥1.47 N copies per nanogram of RNA predicted a positive subgenomic RNA result with 93.0% sensitivity and 91.6% specificity, with a receiver operating characteristic (ROC) area under the curve (AUC) of 0.965 (95% CI: 0.953–0.977; Extended Data Fig. 2f).

We isolated SARS-CoV-2 in Vero E6 cell culture from diverse tissues in and outside the respiratory tract including heart, lymph node, gastrointestinal tract, adrenal gland and eye from early cases (Extended Data Fig. 3a). In total, we isolated virus from 25/55 (45%) specimens tested across four SARS-CoV-2 subgenomic RNA quantification cycle (Cq) value intervals, with decreasing yield with rising Cq interval. Among the 55 samples tested for virus isolation, with sensitivity and specificity weighted equally, a ddPCR value of ≥758 N copies per nanogram of RNA predicted replication-competent virus with 76% sensitivity and 90% specificity (ROC AUC = 0.887; 95% CI: 0.795–0.978), and a subgenomic RNA value of ≥25,069 copies per microlitre of RNA (about Cq 22.40) predicted replication-competent virus with 72% sensitivity and 100% specificity (ROC AUC = 0.915; 95% CI: 0.843–0.987; Extended Data Fig. 3b,c).

We reattempted virus isolation from thalamus and hypothalamus of P38 on Vero E6-TMPRSS2-T2A-ACE2 cells[16] and observed a cytopathic effect 48 h after inoculation with thalamus tissue homogenate from P38. RT–qPCR for SARS-CoV-2 envelope (E) genomic RNA was carried out on the tissue homogenate and the supernatant of the virus isolation process at the time of the cytopathic effect, and yielded Ct values of 27.33 and 13.24, respectively.

Viral genome sequencing

We used HT-SGS to analyse SARS-CoV-2 spike gene variant sequences from a total of 46 tissues in 6 individuals (Extended Data Fig. 4). In P27 (D1), P19 (D7) and P18 (D9), no nonsynonymous virus genetic diversity was detected in respiratory and non-respiratory sites despite a high depth of single-molecule sampling. In P27, two virus haplotypes, each with a single synonymous substitution, were preferentially detected in non-respiratory sites including the right and left ventricles and mediastinal lymph node. In P38 (D13), a D80F residue was identified in 31/31 pulmonary but 0/490 brain sequences, and a G1219V residue was restricted to brain variants. SARS-CoV-2 virus isolated from thalamus of P38 through Vero E6-TEMPRSS2-TA2-ACE2 cell culture and subjected to short-read, whole-genome sequencing matched the minor haplotype detected from P38 RNAlater-preserved thalamus and the major haplotype of P38 RNAlater-preserved hypothalamus. A nonsynonymous substitution was also detected in P36 (D4) dura mater, albeit at very low sampling depth (n = 2 sequences), compared with non-CNS tissue.

ISH reveals the cellular tropism of SARS-CoV-2

We validated our ddPCR results by ISH for SARS-CoV-2 spike RNA in respiratory and non-respiratory tissues in selected early, mid and late cases across >35 cell types and hyaline membranes (Figs. 2 and 3, Extended Data Table 3 and Supplementary Data 3). Detailed annotation of SARS-CoV-2 spike RNA ISH-positive cells by tissue, including across multiple brain regions, is provided in Figs. 2 and 3 and Supplementary Data 3.

To determine the relationship between SARS-CoV-2 N RNA detected by ddPCR and SARS-CoV-2 spike RNA detected by ISH, we carried out

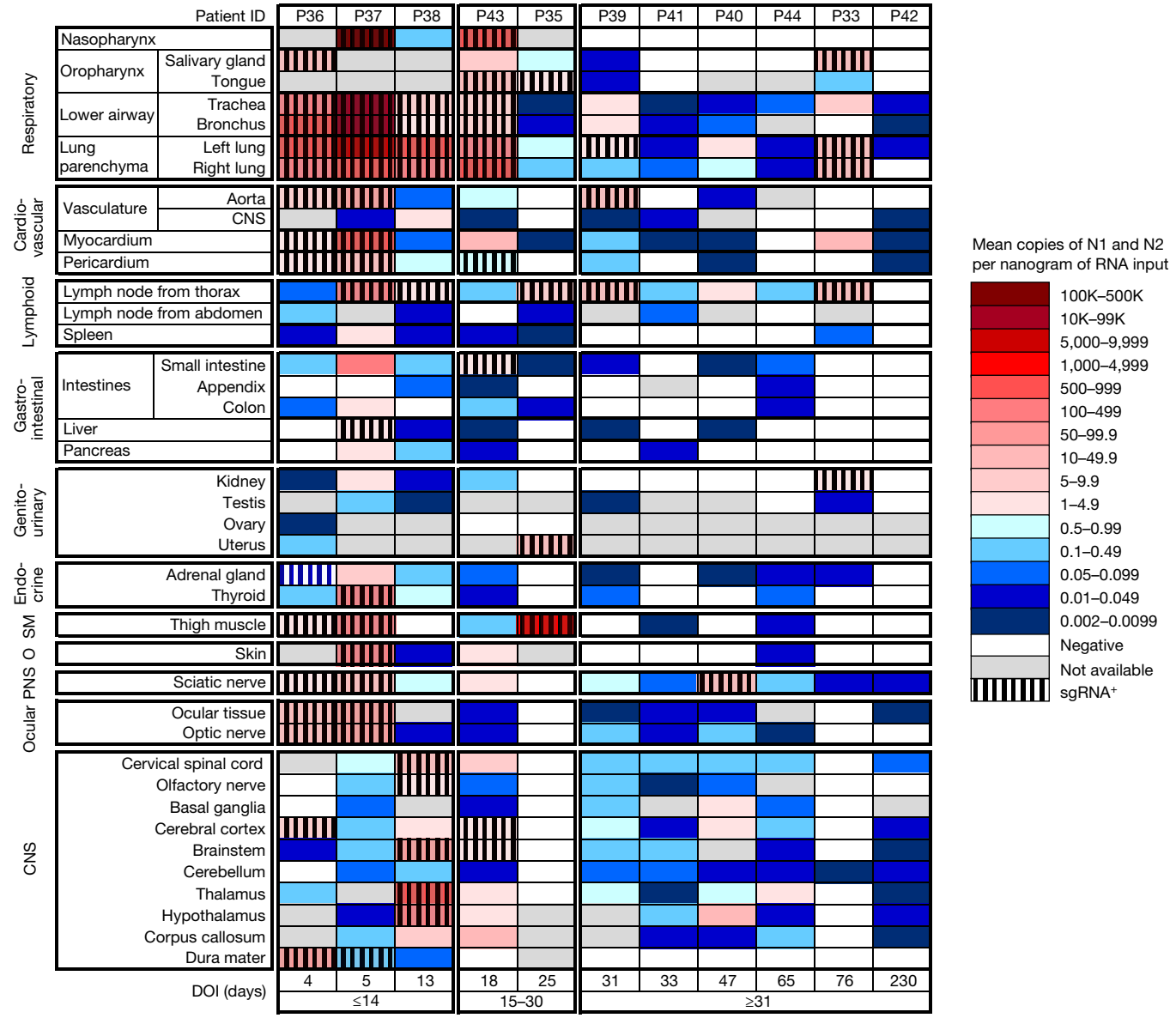

Fig. 1 | Distribution, quantification and replication of SARS-CoV-2 across the human body and brain. The heat map depicts the highest mean quantification of SARS-CoV-2 RNA (N) through ddPCR present in the autopsy tissues of 11 patients who died with COVID-19 and underwent whole-body and brain sampling. Patients are aligned from shortest to longest duration of illness (DOI) before death, listed at the bottom of the figure, and grouped into early (≤14 days), mid (15–30 days) and late (≥31 days) duration of illness. Tissues are organized by tissue group beginning with the respiratory tissues at the top and CNS at the bottom. Viral RNA levels range from 0.002 to 500,000 N gene copies per nanogram of RNA input, depicted as a gradient from dark blue at the lowest level to dark red at the highest level. Tissues that were also positive for subgenomic RNA (sgRNA$^+$) through real-time RT–qPCR are shaded with black vertical bars. O, other; PNS, peripheral nervous system; SM, skeletal muscle.

image analysis on interventricular septal tissue from 16 cases covering a four-log range of SARS-CoV-2 N gene copies per nanogram of RNA ddPCR values. Interventricular septum was selected for this analysis owing to consistent histomorphology. Mean SARS-CoV-2 N gene copies per nanogram of RNA significantly correlated with the median SARS-CoV-2 spike RNA-positive cells over thirty ×40 fields ($\rho = 0.704$, 95% CI: 0.320–0.889, $P = 0.002$; Supplementary Data 3).

SARS-CoV-2 N RNA and protein in CNS

To further validate detection and distribution of SARS-CoV-2 in CNS tissue, we used a second ISH assay targeting N RNA, and IF and chromogenic IHC-based assays targeting N protein. We confirmed the specificity of these assays with appropriate positive and negative controls (Supplementary Data 3, panels yy–bbb) and applied them to selected CNS tissues that were SARS-CoV-2 positive by ddPCR. We observed SARS-CoV-2 RNA and protein in hypothalamus and cerebellum of an early case (P38) and cervical spinal cord and basal ganglia of late cases (P42 and P40, respectively), with a pattern consistent with neuronal staining (Fig. 3).

COVID-19 histological findings

The histopathology findings from our cohort were similar to those reported in other case series (Extended Data Fig. 5). Of 44 cases, 38 were determined to have died from COVID-19, and of these, 35 (92.1%) had either acute pneumonia or diffuse alveolar damage at the time of death (Supplementary Data 2). Phases of diffuse alveolar damage showed a

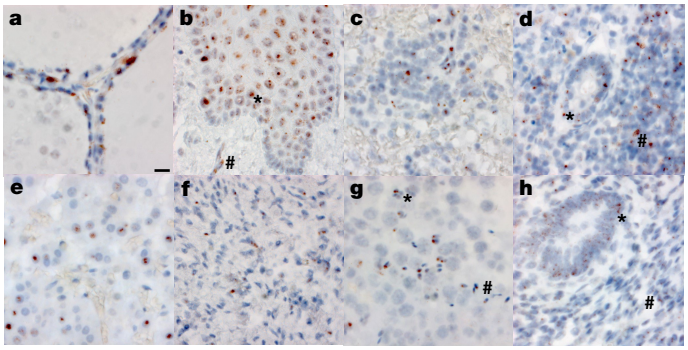

Fig. 2 | RNA in situ (RNAscope) detection of SARS-CoV-2 in extrapulmonary tissues. a–**h**, SARS-CoV-2 virus is localized to the Golgi and endoplasmic reticulum, perinuclear in appearance, in the following organs and cell types (×500 magnifications, scale bars, 2 µm, all panels): thyroid of P19, demonstrating the presence of virus in follicular cells (**a**), oesophagus of P18, demonstrating the presence of virus in the stratified squamous epithelium (asterisk), as well as signal in capillaries within the stroma (hash) (**b**), spleen of P19, demonstrating the presence of virus in mononuclear leukocytes in the white pulp (**c**), appendix of P19, demonstrating the presence of virus in both colonic epithelium (asterisk) and mononuclear leukocytes in the stroma (hash) (**d**), adrenal gland of P19, demonstrating the presence of virus in endocrine secretory cells (**e**), ovary of P18, demonstrating the presence of virus in stromal cells of the ovary in a post-menopausal ovary (**f**), testis of P20, demonstrating the presence of virus in both Sertoli cells (asterisk) and maturing germ cells in the seminiferous tubules of the testis (hash) (**g**), endometrium of P35, demonstrating the presence of virus in endometrial gland epithelium (asterisk) and stromal cells (hash), in a pre-menopausal endometrial sample (**h**). The images are exemplars of extrapulmonary tissues that were positive for SARS-CoV-2 N RNA during 20 batches of ISH staining.

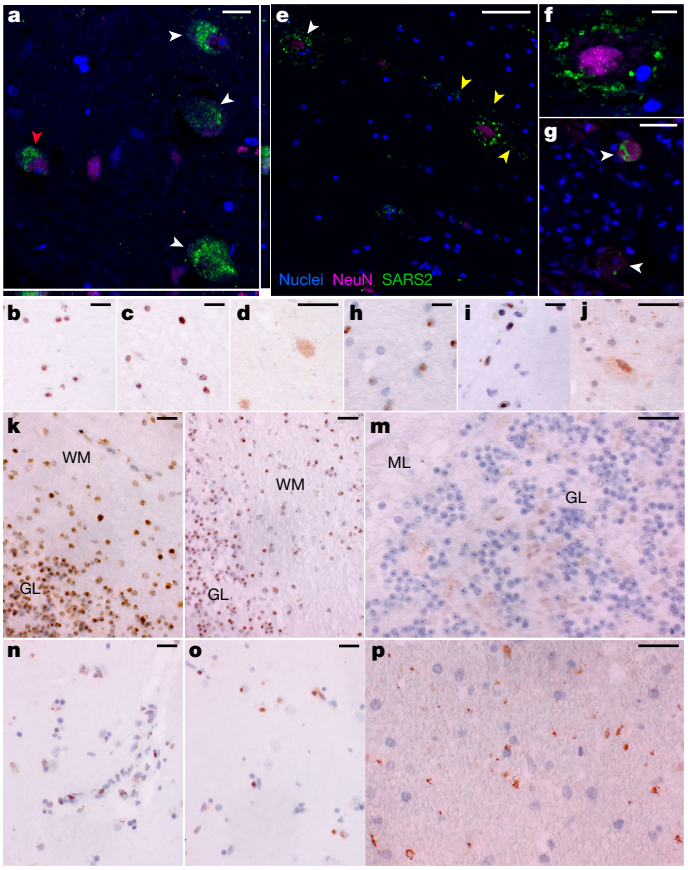

Fig. 3 | SARS-CoV-2 protein and RNA expression in human CNS tissues. a, High-magnification visualization of hypothalamus from P38 labelled for SARS-CoV-2 N protein (green) and neuronal nuclear (NeuN) protein (magenta), demonstrating viral-specific protein expression in neurons (white arrowheads) by IF. *The z*-stack orthogonal views to the right and bottom of **a** demonstrate NeuN labelling in the nucleus and SARS-CoV-2 protein in the cytoplasm of the cell (red arrowhead). **b**–**d**, SARS-CoV-2 spike (S) (**b**) and N (**c**) RNA (brown) by ISH and SARS-CoV-2 N (**d**) protein (brown) by chromogenic IHC of hypothalamus of P38. **e**, Infected neurons were found in the cervical spinal cord of P42 by IF, for which white arrowheads indicate NeuN-positive neurons with associated virus protein. Viral protein labelling was also identified in linear structures radiating away from neuronal cell bodies suggestive of neuronal projections (yellow arrowheads). **f**, A higher magnification of neuron-associated viral protein labelling. **g**, Viral protein was also detected by IF in neurons of the spinal ganglia at the level of the cervical spinal cord of P42 (white arrowheads). **h**–**j**, SARS-CoV-2 S (**h**) and N (**i**) RNA by ISH and SARS-CoV-2 N (**j**) protein by chromogenic IHC of cervical spinal cord of P42. **k**–**m**, SARS-CoV-2 S (**k**) and N (**l**) RNA by ISH and SARS-CoV-2 N (**m**) protein by chromogenic IHC, all of which are predominantly found in the granular layer (GL) as compared to the molecular level (ML) of cerebellum of P38. WM, white matter. **n**,**o**, SARS-CoV-2 S (**n**) and N (**o**) RNA by ISH and SARS-CoV-2 N (**p**) viral protein by chromogenic IHC of basal ganglia of P40. Hoechst 33342 was used to identify nuclei (blue) in all IF images, and IF images were obtained by confocal microscopy. Haematoxylin was used as a counterstain and all ISH and chromogenic IHC images were obtained by bright-field microscopy. Scale bars, 15 µm (**a**), 10 µm (**b**–**d**,**g**–**p**) and 25 µm (**e**,**f**).

clear temporal progression (Extended Data Fig. 6). Pulmonary thromboembolic complications were noted in 10 (23%) cases and myocardial infiltrates were observed in four cases, including one case of substantial myocarditis[17] (P3). In the lymph nodes and spleen, we observed both lymphodepletion and follicular and paracortical hyperplasia.

Other non-respiratory histological changes were mainly related to complications of therapy or pre-existing comorbidities. Five cases had old ischaemic myocardial scars and three had coronary artery bypass grafts in place. Diabetic nephropathy and steatohepatitis were observed in ten cases (23%) and five cases (12%), respectively. One case had known hepatitis C with cirrhosis, but the other cases of advanced hepatic fibrosis were probably related to fatty liver disease. Hepatic necrosis (13 cases, 30%) and changes consistent with acute kidney injury (17 cases, 39%) were probably related to hypoxic–ischaemic injury in these very ill patients.

In the examination of 11 brains, we found few histopathologic changes, despite substantial viral burden. Vascular congestion was an unusual finding that had an unclear aetiology and could be related to the haemodynamic changes incurred with infection. Global hypoxic–ischaemic change was seen in two cases, one of which was a juvenile (P36) with a seizure disorder who was found to be SARS-CoV-2 positive on hospital admission, but who probably died of seizure complications unrelated to viral infection.

Discussion

Here we provide, to our knowledge, the most comprehensive analysis to date of the cellular tropism, quantification and persistence of SARS-CoV-2 across the human body including the brain. Our focus on short postmortem intervals, a comprehensive standardized approach to tissue collection, dissecting the brain before fixation, preserving tissue in RNAlater and flash freezing of fresh tissue allowed us to detect and quantify SARS-CoV-2 RNA levels with high sensitivity by ddPCR and ISH, as well as isolate virus in cell culture from multiple non-respiratory tissues including the brain, which are notable differences compared to other studies.

We show that SARS-CoV-2 disseminates early in infection in some patients, with a significantly higher viral burden in respiratory than non-respiratory tissues. We demonstrated virus replication in multiple non-respiratory sites during the first two weeks following symptom onset and detected subgenomic RNA in at least one tissue in 14 of 27 cases beyond D14, indicating that viral replication may occur

in non-respiratory tissues for several months. Whereas others have proposed that the detection of SARS-CoV-2 in non-respiratory tissues might be due to residual blood within tissues[8,18] or cross-contamination from the lungs during tissue procurement[8], our data indicate otherwise. Specifically, only 12 of our cases had detectable SARS-CoV-2 RNA in a perimortem plasma sample, only 2 cases had SARS-CoV-2 subgenomic RNA detected in plasma, and negligible, if any, RNA was detected in banked peripheral blood mononuclear cells from representative cases. Further, we validated detection of SARS-CoV-2 outside the respiratory tract by direct cellular identification of virus in cells through ISH, IHC and IF, isolation of SARS-CoV-2 by cell culture, and detection of distinct SARS-CoV-2 spike sequence variants in non-respiratory sites.

Others have previously reported SARS-CoV-2 RNA within the heart, lymph node, small intestine and adrenal gland[6,8–12,18]. We replicate these findings and conclusively demonstrate that SARS-CoV-2 is capable of infecting and replicating within these and many other tissues, including brain. Specifically, we report the recovery of replication-competent SARS-CoV-2 from thalamus of P38 at D13 using a modified Vero E6 cell line that stably expresses ACE2 and TMPRSS2. This along with detection of genomic RNA and subgenomic RNA through PCR, multiple imaging modalities showing SARS-CoV-2 RNA and protein within cells of the CNS, and distinct minor variants detected through sequencing in the CNS prove definitively that SARS-CoV-2 is capable of infecting and replicating within the human brain.

HT-SGS of SARS-CoV-2 spike demonstrates homogeneous virus populations in many tissues, while also revealing informative virus variants in others. Low intra-individual diversity of SARS-CoV-2 sequences has been observed frequently in previous studies[19–21], and probably relates to the intrinsic mutation rate of the virus as well as lack of early immune pressure to drive virus evolution. It is important to note that our HT-SGS approach has both a high accuracy and a high sensitivity for minor variants within each sample, making findings of low virus diversity highly reliable[22]. Genetic compartmentalization of SARS-CoV-2 between respiratory and non-respiratory tissues in several individuals supports independent replication of the virus at these sites, although lack of compartmentalization between sites does not rule out independent virus replication. We note several cases in which brain-derived virus spike sequences showed nonsynonymous changes relative to sequences from other non-CNS tissues. Further studies will be needed to understand whether these cases might represent stochastic seeding of the CNS or differential selective pressure on spike by antiviral antibodies in the CNS, as others have suggested[23–25].

Our results show that although the highest burden of SARS-CoV-2 is in respiratory tissues, the virus can disseminate throughout the entire body. Whereas others have posited that this viral dissemination occurs through cell trafficking[11] due to a reported failure to culture SARS-CoV-2 from blood[3,26], our data support an early viraemic phase, which seeds the virus throughout the body following infection of the respiratory tract. Recent work[26] in which SARS-CoV-2 virions were pelleted and imaged from plasma of patients with acute COVID-19 supports this mechanism of viral dissemination. Our cohort is predominantly composed of severe and ultimately fatal COVID-19 cases. However, two cases (P36 and P42) reported only mild or no respiratory symptoms and died with, not from, COVID-19, yet had SARS-CoV-2 RNA widely detected across the body and brain. Additionally, P36 was a juvenile with an underlying neurological condition, but without evidence of multisystem inflammatory syndrome in children, suggesting that children may develop systemic infection with SARS-CoV-2 without developing a generalized inflammatory response.

Finally, our work begins to elucidate the duration and locations at which SARS-CoV-2 RNA can persist. Although the respiratory tract was the most common location in which SARS-CoV-2 RNA persisted, ≥50% of late cases also had persistent RNA in the myocardium, lymph nodes from the head and neck and from the thorax, sciatic nerve, ocular tissue, and in all sampled regions of the CNS, except the dura mater. Notably, despite having more than 100 times higher SARS-CoV-2 RNA in respiratory compared to non-respiratory tissues in early cases, this difference greatly diminished in late cases. Less efficient viral clearance in non-respiratory tissues may be related to tissue-specific differences in the ability of SARS-CoV-2 to alter cellular detection of viral mRNA, interfere with interferon signalling, or disrupt viral antigen processing and presentation[27–29]. Understanding mechanisms by which SARS-CoV-2 evades immune detection is essential to guide future therapeutic approaches to facilitate viral clearance.

We detected subgenomic RNA in tissue from more than 60% of the cohort, including in multiple tissues of a case at D99. Although subgenomic RNA is generated during active viral replication, it is less definitive than cell culture at demonstrating replication-competent virus because subgenomic RNA is protected by double-membrane vesicles that contribute to nuclease resistance and longevity beyond immediate viral replication[30–33]. However, nonhuman primates exposed to γ-irradiated SARS-CoV-2 inoculum with high subgenomic RNA copy numbers through multiple mucosal routes had detectable SARS-CoV-2 genomic RNA but undetectable subgenomic RNA levels in respiratory samples by day 1 post-inoculation[15]. These data suggest that detection of SARS-CoV-2 subgenomic RNA probably reflects recent viral replication. Prolonged detection of subgenomic RNA in a subset of our cases may, however, represent defective rather than productive viral replication, which has been described in persistent infection with measles virus—another single-strand enveloped RNA virus—in cases of subacute sclerosing panencephalitis[34].

Our study has several important limitations. First, our cohort largely represents older unvaccinated individuals with pre-existing medical conditions who died from severe COVID-19, limiting our ability to extrapolate findings to younger, healthier or vaccinated individuals. Second, our cases occurred during the first year of the pandemic, before widespread circulation of variants of concern, and thus findings might not be generalizable to current and future SARS-CoV-2 variants. Finally, although it is tempting to attribute clinical findings observed in post-acute sequelae of SARS-CoV-2 to viral persistence, our study was not designed to address this question. Despite these limitations, our findings fundamentally improve the understanding of SARS-CoV-2 cellular distribution and persistence in the human body and brain and provide a strong rationale for pursuing future similar studies to define mechanisms of SARS-CoV-2 persistence and contribution to post-acute sequelae of SARS-CoV-2.

Online content

Any methods, additional references, Nature Portfolio reporting summaries, source data, extended data, supplementary information, acknowledgements, peer review information; details of author contributions and competing interests; and statements of data and code availability are available at https://doi.org/10.1038/s41586-022-05542-y.

1. Bourgonje, A. R. et al. Angiotensin-converting enzyme 2 (ACE2), SARS-CoV-2 and the pathophysiology of coronavirus disease 2019 (COVID-19). *J. Pathol.* **251**, 228–248 (2020).
2. Salamanna, F., Maglio, M., Landini, M. P. & Fini, M. Body localization of ACE-2: on the trail of the keyhole of SARS-CoV-2. *Front. Med.* **7**, 594495 (2021).
3. Sridhar, S. & Nicholls, J. Pathophysiology of infection with SARS-CoV-2—what is known and what remains a mystery. *Respirology* **26**, 652–665 (2021).
4. Al-Aly, Z., Xie, Y. & Bowe, B. High-dimensional characterization of post-acute sequelae of COVID-19. *Nature* **594**, 259–264 (2021).
5. Crook, H., Raza, S., Nowell, J., Young, M. & Edison, P. Long covid-mechanisms, risk factors, and management. *Brit. Med. J.* **374**, n1648 (2021).
6. Puelles, V. G. et al. Multiorgan and renal tropism of SARS-CoV-2. *N. Engl. J. Med.* **383**, 590–592 (2020).
7. Martines, R. B. et al. Pathology and pathogenesis of SARS-CoV-2 associated with fatal coronavirus disease, United States. *Emerg. Infect. Dis.* **26**, 2005–2015 (2020).
8. Bhatnagar, J. et al. Evidence of severe acute respiratory syndrome coronavirus 2 replication and tropism in the lungs, airways, and vascular endothelium of patients with fatal coronavirus disease 2019: an autopsy case series. *J. Infect. Dis.* **223**, 752–764 (2021).
9. Dorward, D. A. et al. Tissue-specific immunopathology in fatal COVID-19. *Am. J. Respir. Crit. Care Med.* **203**, 192–201 (2021).

10. Schurink, B. et al. Viral presence and immunopathology in patients with lethal COVID-19: a prospective autopsy cohort study. *Lancet Microbe* **1**, e290–e299 (2020).
11. Yao, X. H. et al. A cohort autopsy study defines COVID-19 systemic pathogenesis. *Cell Res.* **31**, 836–846 (2021).
12. Remmelink, M. et al. Unspecific post-mortem findings despite multiorgan viral spread in COVID-19 patients. *Crit. Care* **24**, 495 (2020).
13. Mukerji, S. S. & Solomon, I. H. What can we learn from brain autopsies in COVID-19. *Neurosci. Lett.* **742**, 135528 (2021).
14. Matschke, J. et al. Neuropathology of patients with COVID-19 in Germany: a post-mortem case series. *Lancet Neurol.* **19**, 919–929 (2020).
15. Speranza, E. et al. Single-cell RNA sequencing reveals SARS-CoV-2 infection dynamics in lungs of African green monkeys. *Sci. Transl. Med.* **13**, eabe8146 (2021).
16. Matsuyama, S. et al. Enhanced isolation of SARS-CoV-2 by TMPRSS2-expressing cells. *Proc. Natl Acad. Sci. USA* **117**, 7001–7003 (2020).
17. Vannella, K. M. et al. Evidence of SARS-CoV-2-specific T-cell-mediated myocarditis in a MIS-A case. *Front. Imunol.* **12**, 779026 (2021).
18. Desai, N. et al. Temporal and spatial heterogeneity of host response to SARS-CoV-2 pulmonary infection. *Nat. Commun.* **11**, 6319 (2020).
19. Tonkin-Hill, G. et al. Patterns of within-host genetic diversity in SARS-CoV-2. *Elife* **10**, e66857 (2021).
20. Lythgoe, K. A. et al. SARS-CoV-2 within-host diversity and transmission. *Science* **372**, eabg0821 (2021).
21. Valesano, A. L. et al. Temporal dynamics of SARS-CoV-2 mutation accumulation within and across infected hosts. *PLoS Pathog.* **17**, e1009499 (2021).
22. Ko, S. H. et al. High-throughput, single-copy sequencing reveals SARS-CoV-2 spike variants coincident with mounting humoral immunity during acute COVID-19. *PLoS Pathog.* **17**, e1009431 (2021).
23. Brioschi, S. et al. Heterogeneity of meningeal B cells reveals a lymphopoietic niche at the CNS border. *Science* **373**, eabf9277 (2021).
24. Wang, Y. et al. Early developing B cells undergo negative selection by central nervous system-specific antigens in the meninges. *Immunity.* **54**, 2784–2794 (2021).
25. Song, E. et al. Divergent and self-reactive immune responses in the CNS of COVID-19 patients with neurological symptoms. *Cell Rep. Med.* **2**, 100288 (2021).
26. Jacobs, J. L. et al. SARS-CoV-2 viremia is associated with COVID-19 severity and predicts clinical outcomes. *Clin. Infect. Dis.* **10**, ciab686 (2021).
27. Wong, L. R. & Perlman, S. Immune dysregulation and immunopathology induced by SARS-CoV-2 and related coronaviruses – are we our own worst enemy? *Nat. Rev. Immunol.* **22**, 47–56 (2022).
28. Diamond, M. S. & Kanneganti, T. D. Innate immunity: the first line of defense against SARS-CoV-2. *Nat. Immunol.* **23**, 165–176 (2022).
29. Beyer, D. K. & Forero, A. Mechanisms of antiviral immune evasion of SARS-CoV-2. *J. Mol. Biol.* **434**, 167265 (2022).
30. Binnicker, M. J. Can testing predict SARS-CoV-2 infectivity? The potential for certain methods to be surrogates for replication-competent virus. *J. Clin. Microbiol.* **59**, e0046921 (2021).
31. Alexandersen, S., Chamings, A. & Bhatta, T. R. SARS-CoV-2 genomic and subgenomic RNAs in diagnostic samples are not an indicator of active replication. *Nat. Commun.* **11**, 6059 (2020).
32. van Kampen, J. et al. Duration and key determinants of infectious virus shedding in hospitalized patients with coronavirus disease-2019. *Nat. Commun.* **12**, 267 (2021).
33. Dimcheff, D. E. et al. Severe acute respiratory syndrome coronavirus 2 total and subgenomic RNA viral load in hospitalized patients. *J. Infect. Dis.* **224**, 1287–1293 (2021).
34. Sidhu, M. S. et al. Defective measles virus in human subacute sclerosing panencephalitis brain. *Virology* **202**, 631–641 (1994).

NIH COVID-19 Autopsy Consortium

Daniel S. Chertow[1,2], Kevin M. Vannella[1,2], Sydney R. Stein[1,2], Marcos J. Ramos-Benitez[1,2,11], Andrew P. Platt[1,2], James M. Dickey[1,2], Ashley L. Babyak[1,2], Luis J. Perez Valencia[1,2], Sabrina C. Ramelli[3], Shelly J. Curran[3], Mary E. Richert[3], Alison Grazioli[4], David E. Kleiner[5], Stephen M. Hewitt[5], Martha Quezado[5], Willie J. Young[5], Sarah P. Young[5], Billel Gasmi[5], Michelly Sampaio De Melo[5], Sabina Desar[5], Saber Tadros[5], Nadia Nasir[5], Xueting Jin[5], Sharika Rajan[5], Esra Dikoglu[5], Neval Ozkaya[5], Kris Ylaya[5], Joon-Yong Chung[5], Stefania Pittaluga[5], Grace Smith[5], Elizabeth R. Emanuel[21], Brian L. Kelsall[21], Justin A. Olivera[22], Megan Blawas[22], Robert A. Star[22], Nicole Hays[10], Madeleine Purcell[10], Shreya Singireddy[10], Jocelyn Wu[10], Katherine Raja[10], Ryan Curto[10], Jean E. Chung[23], Amy J. Borth[23], Kimberly A. Bowers[23], Anne M. Weichold[23], Paula A. Minor[23], Mir Ahmad N. Moshref[23], Emily E. Kelly[23], Mohammad M. Sajadi[14,15], Kapil K. Saharia[14,15], Daniel L. Herr[12], Thomas M. Scalea[24], Douglas Tran[16], Ronson J. Madathil[16], Siamak Dahi[16], Kristopher B. Deatrick[16], Eric M. Krause[25], Joseph Rabin[13], Joseph A. Herrold[17], Ali Tabatabai[17], Eric S. Hochberg[17], Christopher R. Cornachione[17], Andrea R. Levine[17], Justin E. Richards[26], John Elder[27], Allen P. Burke[27], Michael A. Mazzeffi[28], Robert H. Christenson[29], Zackary A. Chancer[30], Mustafa Abdulmahdi[31], Sabrina Sopha[31], Tyler Goldberg[31], Shahabuddin Soherwardi[18], Yashvir Sangwan[32], Michael T. McCurdy[17,19], Kristen Sudano[19], Diane Blume[19], Bethany Radin[19], Madhat Arnouk[19], James W. Eagan Jr[33], Robert Palermo[34], Anthony D. Harris[35], Thomas Pohida[36], Marcial Garmendia-Cedillos[36], George Dold[37], Eric Saglio[37] & Phuoc Pham[37]

[21]Mucosal Immunobiology Section, Laboratory of Molecular Immunology, National Institute of Allergy and Infectious Diseases, National Institutes of Health, Bethesda, MD, USA. [22]Renal Diagnostics and Therapeutics Unit, Kidney Diseases Branch, National Institute of Diabetes and Digestive and Kidney Diseases, National Institutes of Health, Bethesda, MD, USA. [23]University of Maryland Medical Center, Baltimore, MD, USA. [24]Department of Shock Trauma Critical Care, University of Maryland School of Medicine, Baltimore, MD, USA. [25]Department of Surgery, Division of Thoracic Surgery, University of Maryland School of Medicine, Baltimore, MD, USA. [26]Department of Anesthesiology, Division of Critical Care Medicine, University of Maryland School of Medicine, Baltimore, MD, USA. [27]Department of Autopsy and Thoracic Pathology, University of Maryland School of Medicine, Baltimore, MD, USA. [28]Department of Anesthesiology and Critical Care Medicine, George Washington University School of Medicine and Health Sciences, Washington, D.C., USA. [29]Department of Laboratory Science, University of Maryland School of Medicine, Baltimore, MD, USA. [30]Department of Anesthesiology, Keck School of Medicine, University of Southern California, Los Angeles, CA, USA. [31]Critical Care Medicine, University of Maryland Baltimore Washington Medical Center, Glen Burnie, MD, USA. [32]Department of Interventional Pulmonology, TidalHealth Peninsula Regional, Salisbury, MD, USA. [33]Department of Pathology, University of Maryland St. Joseph Medical Center, Towson, MD, USA. [34]Department of Pathology, Greater Baltimore Medical Center, Townson, MD, USA. [35]Department of Epidemiology and Public Health, University of Maryland School of Medicine, Baltimore, MD, USA. [36]Instrumentation Development and Engineering Application Solutions, National Institute of Biomedical Imaging and Bioengineering, National Institutes of Health, Bethesda, MD, USA. [37]Section on Instrumentation, National Institute of Mental Health, National Institutes of Health, Bethesda, MD, USA.

Methods

Autopsies

Autopsies were carried out and tissues were collected as previously described[35] in the National Cancer Institute's Laboratory of Pathology at the National Institutes of Health Clinical Center following consent of the legal next of kin. Autopsy patients in this cohort were unvaccinated against SARS-CoV-2. Tissues preserved for histopathologic analysis and special staining were dissected fresh at the time of autopsy, placed into tissue cassettes, fixed for 24 h in neutral-buffered formalin, and then transferred to 70% ethanol for 48 h before impregnation with paraffin.

Measurement of IgG and IgM antibodies to N and spike protein of SARS-CoV-2

Fluid-phase luciferase immunoprecipitation system assays were used to study IgG and IgM antibody response to SARS-CoV-2. For IgG luciferase immunoprecipitation system measurements, *Renilla* luciferase–nucleocapsid and *Gaussia* luciferase–spike protein extracts were used with protein A/G beads (Protein A/G UltraLink Resin, Thermo Fisher) as the IgG capture reagent as previously described with microtitre filter plates[36]. For IgM measurements, anti-human IgM goat agarose beads (Sigma) were substituted as the capture reagent using both the microfilter plate and microtube format[37]. The IgM immunoprecipitation assays were carried out in 1.5-ml microfuge tube format containing 1 µl serum or plasma, *Renilla* luciferase–N (10 million light unit input per tube) or *Gaussia* luciferase–spike protein (40 million light input per tube) and buffer A (20 mM Tris, pH 7.5, 150 mM NaCl, 5 mM $MgCl_2$, 0.1% Triton X-100) to a total volume of 100 µl. After mixing, the tubes were incubated at room temperature for 1 h. Next, 10 µl of the anti-human IgM agarose bead suspension was added to each tube for a further 60 min, and tubes were placed on a rotating wheel at 4 °C. The samples were then washed by brief centrifugation to collect the bead pellet at room temperature three times with 1.5 ml buffer A and once with 1.5 ml PBS. After the final wash, the beads were mixed with coelenterazine substrate (100 µl) and light units were measured in a tube luminometer. Known seronegative and seropositive samples for IgG and IgM antibodies to the N and spike proteins were used for assigning seropositive cutoff values and for standardization.

SARS-CoV-2 RNA quantification of tissues and body fluids

Total RNA was extracted from RNAlater (Invitrogen)-preserved tissues and body fluids collected at autopsy using the RNeasy Mini, RNeasy Fibrous Tissue Mini, RNeasy Lipid Tissue Mini and QIAamp Viral RNA Mini Kits (Qiagen) according to the manufacturer's protocols. Upstream tissue processing and subsequent RNA quantification have been described previously[35]. The QX200 AutoDG Droplet Digital PCR System (Bio-Rad) was used to detect and quantify SARS-CoV-2 RNA in technical replicates of 5.5 µl RNA for fluids and up to 550 ng RNA for tissues. Raw data were collected using QuantaSoft version 1.7.4.0917 and analysed using QuantaSoft Analysis Pro version 1.0.596. Results were then normalized to copies of N1, N2 and RP per millilitre of sample input for fluids and per nanogram of RNA concentration input for tissues. Samples had to be positive for the human RNase P (RP) gene at the manufacturer's limit of detection (LOD) of ≥0.2 copies per microlitre and ≥4 positive droplets per well to ensure RNA extraction was successful and be reported. For samples to be considered positive for SARS-CoV-2 N1 or N2 genes, the technical replicates needed to have an average at or above the manufacturer's LOD of ≥0.1 copies per microlitre and ≥2 positive droplets per well. More than 60 control autopsy tissues from uninfected individuals, representing all organs collected for COVID-19 autopsy cases, were used to validate the manufacturer's emergency use authorization published LOD for nasopharyngeal swabs for tissues (Supplementary Data 1e). ddPCR data for P3 (ref. [17]) as well as a portion of the oral cavity[35] have been reported previously.

Subgenomic RNA analysis of ddPCR positive tissues

Tissues that tested positive for one or both SARS-CoV-2 N gene targets through ddPCR had RNA submitted for subgenomic RNA analysis. Briefly, 5 µl of sample RNA was added to a one-step real-time RT–qPCR assay targeting subgenomic RNA of the envelope (E) gene (forward primer 5′-CGATCTCTTGTAGATCTGTTCTC-3′; reverse primer 5′-ATATTGCAGCAGTACGCACACA-3′; probe 5′-FAM-ACACTAGCCATCCTTACTGCGCTTCG-ZEN-IBHQ-3′)[38] using the Rotor-Gene probe kit (Qiagen) according to instructions of the manufacturer. In each run, standard dilutions of counted RNA standards were run in parallel to calculate copy numbers in the samples. The LOD for this assay was determined to be <40 Cq (Supplementary Data 1) using 40 control autopsy tissues from uninfected individuals, representing all organs collected for COVID-19 autopsy cases.

Virus isolation from select postmortem tissues

Select tissues with high viral RNA levels through ddPCR and subgenomic RNA RT-qPCR measuring across a broad range of 16 to <35 Cq underwent virus isolation to prove the presence of infectious virus. Virus isolation was carried out on tissues by homogenizing the tissue in 1 ml DMEM and inoculating Vero E6 cells in a 24-well plate with 250 µl of cleared homogenate and a 1:10 dilution thereof. Plates were centrifuged for 30 min at 1,000 r.p.m. and incubated for 30 min at 37 °C and 5% CO_2. The inoculum was then removed and replaced with 500 µl DMEM containing 2% FBS, 50 U ml^{-1} penicillin and 50 µg ml^{-1} streptomycin. Six days after inoculation, the cytopathic effect was scored. A blind passage of samples in which no cytopathic effect was present was carried out according to the same method. Additional virus isolation from P38 thalamus and hypothalamus was carried out using Vero E6-TMPRSS2-T2A-ACE2 (catalogue no. NR-54970, BEI Resources) grown in DMEM containing 10% FBS, 50 U ml^{-1} penicillin, 50 µg ml^{-1} streptomycin and 10 µg ml^{-1} puromycin. Virus isolation was carried out as described for other tissues on Vero E6 cells, without selection antibiotics. Tissue homogenate from flash-frozen specimens and supernatants from plates were analysed using RT–qPCR for SARS-CoV-2 E gene subgenomic RNA (described above) or genomic RNA as previously described[39] to rule out other causes for the cytopathic effect. Cell lines were not authenticated in house, but were confirmed to be free of mycoplasma contamination.

Virus sequencing

Five early cases (P18, P19, P27 and P38) and one late case (P33) with multiple body site tissues containing subgenomic RNA levels ≤31 Cq were selected for HT-SGS as previously described[22]. Presence of variants of SARS-CoV-2 was analysed within and between tissues.

Supernatant from the virus isolation plates of thalamus of P38 were sequenced using short-read, whole-genome sequencing. Total RNA was depleted of rRNA using Ribo-Zero+ following the manufacturer's protocol (Illumina). Cleaned RNA was eluted in water and sequencing libraries were prepared following the Kapa RNA HyperPrep kit according to the manufacturer's protocol (Roche Sequencing Solutions). Briefly, 10 µl of depleted RNA was used as a template for fragmentation (65 °C for 1 min) and first-strand synthesis. To facilitate multiplexing, adapter ligation was carried out with KAPA Unique Dual-Indexed Adapters, and samples were enriched for adapter-ligated product using KAPA HiFi HotStart Ready mix and a range of 9–19 PCR amplification cycles based on SARS-CoV-2 Ct values and total RNA starting inputs. Pools consisting of 1–6 sample libraries were used for hybrid-capture virus enrichment using myBaits Expert Virus SARS-CoV-2 panel following the manufacturer's manual, version 5.01, with a range of 12–18 cycles of post-capture PCR amplification (Arbor Biosciences). Purified, enriched libraries were quantified on a CFX96 Real-Time System (Bio-Rad) using Kapa Library Quantification kit (Roche Sequencing Solutions). Libraries were diluted to 2 nM stock, pooled together as needed in equimolar concentrations and sequenced on the MiSeq (Illumina) generating

2 × 150-bp paired-end reads. Raw sequence reads were trimmed of Illumina adapter sequence using Cutadapt version 1.12 (ref. [40]) and then trimmed and filtered for quality using the fastq_quality_trimmer and fastq_quality_filter tools from the FASTX-Toolkit 0.0.14 (Hannon Lab, CSHL). Reads were then mapped to the SARS-CoV-2 2019-nCoV/USA-WA1/2020 genome (MN985325.1) using Bowtie2 version 2.2.9 (ref. [41]) with parameters -local -no-mixed -X 1500. PCR duplicates were removed using picard MarkDuplicates, version 2.26.10 (Broad Institute).

SARS-CoV-2 RNA ISH

Chromogenic ISH detection was carried out using the manual RNAScope 2.5 HD assay (catalogue no. 322310, Advanced Cell Diagnostics) with a modified pretreatment protocol. Briefly, formalin-fixed and paraffin-embedded (FFPE) tissue sections were cut at 7 µm, air dried overnight, and baked for 1–2 h at 60 °C. The FFPE tissue sections were deparaffinized, dehydrated and then treated with pretreat 1 for 15 min at room temperature. The slides were boiled with pretreatment reagent for 15 min, digested with protease at 40 °C for 20 min, and then hybridized for 2 h at 40 °C with probe-V-nCov2019-S (catalogue no. 848561, Advanced Cell Diagnostics) or probe-V-nCoV-N (catalogue no. 846081, Advanced Cell Diagnostics)[42]. In addition, probe-Hs-PPIB (peptidylprolyl isomerase B, catalogue no. 313901, Advanced Cell Diagnostics) and probe-dapB (catalogue no. 310043, Advanced Cell Diagnostics) were used as a positive and negative control, respectively. Subsequent amplification was carried out according to the original protocol. Detection of specific probe-binding sites was visualized with RNAScope 2.5 HD Reagent Kit-BROWN chromogenic labels (Advanced Cell Diagnostics). The slides were counterstained with haematoxylin and coverslipped.

To correlate viral load detected between ddPCR and ISH, the interventricular septum of 16 cases spanning a four-log range of SARS-CoV-2 N copies per nanogram of RNA through ddPCR underwent ISH and subsequent quantification using image analysis. The interventricular septum stained slides were digitalized using a NanoZoomer XR Digital Pathology system (Hamamatsu, Hamamatsu City, Japan) at 40× magnification. Digitalized images were automatically analysed using Visiopharm software v2021.09.02 (Visiopharm, Hørsholm, Denmark). A training set was used to configure the algorithm and identify SARS-CoV-2 RNA signals. In brief, 3,3′-diaminobenzidine (DAB) dots of positive signals were identified using a Bayesian classifier trained on pre-processing steps. We randomly selected 30 regions of interest per slide and calculated the median of positive cells.

SARS-CoV-2 multiplex IF

FFPE CNS sections were deparaffinized, rehydrated and subjected to 0.01 M citrate buffer antigen retrieval for 20 min at 120 °C. Slides were then rinsed briefly in deionized water, washed with PBS and subsequently incubated in a 5% milk (catalogue no. 1706404, Bio-Rad), 5% normal donkey serum, 0.3 M glycine and 0.1% Triton X-100 blocking solution made up in PBS for 30 min. Primary antibodies to SARS-CoV-2 N protein 1 (NP1, 1:1,000, custom made GenScript U864YFA140-4/CB2093)[43–45] and neuronal nuclear protein (NeuN, 1:200, catalogue no. MAB377, Chemicon) or transmembrane protein 119 (TMEM119, 1:1,000, catalogue no. MAB130313, R&D Systems) were diluted in blocking serum and applied to slides overnight at 4 °C. The following day, slides were washed extensively with PBS to remove any detergent and freshly made True Black Plus solution (1:40 in PBS, catalogue no. 23014, Biotium) was applied for 14 min. Slides were again extensively washed and then species-specific secondary conjugates (1:500, catalogue nos. A-21206 and A-21203, Thermo Fisher) were applied for 1 h at room temperature. Following PBS wash, Hoechst 33342 was applied for 10 min (1:2,000, catalogue no. H3570, Thermo Fisher) to label nuclei. Slides were coverslipped with Prolong Gold (catalogue no. P36930, Thermo Fisher).

SARS-CoV-2 chromogenic IHC

Chromogenic IHC was carried out on various ddPCR positive CNS and lung tissues and negative pre-pandemic control cases demonstrating relative expression of the target protein between infected and control samples. Briefly, 5 µm FFPE tissue sections were incubated at 60 °C for 2 h, deparaffinized in xylene, and hydrated in serial alcohol solutions to distilled water. Heat antigen retrieval was carried out using a pressure cooker (DAKO) by submerging slides in 1× pH 6 citrate buffer for 20 min. Endogenous enzyme activity was quenched with 3% hydrogen peroxide containing sodium azide for 10 min with additional 10% non-fat dry milk (Bio-Rad) for 20 min to prevent nonspecific binding. Tissue sections were then incubated with polyclonal SARS or SARS-CoV-2 N antibody (1:500, custom made, GenScript U864YFA140-4/CB2093, 0.447 mg ml^{-1})[43–45] for 1 h at room temperature. Negative controls were congruently stained on subsequent sections following the same protocol replacing the primary antibody with a rabbit IgG control antibody (0.5 mg ml^{-1}, catalogue no. I-1000-5, Vector Laboratories). The antigen–antibody reaction was detected with Dako Envision+Rb polymer detection system (DAKO) and visualized with DAB chromogen. Sections were lightly counterstained with haematoxylin, dehydrated in graded alcohols, cleared in xylene, mounted and coverslipped.

Statistical analysis

Correlations between two continuous variables were assessed using Spearman's rank correlation coefficient (ρ). Fisher's z-transformation was used for the calculations of 95% CI and P values. To compare ddPCR levels between tissue types (respiratory versus non-respiratory), we used linear mixed models with compound symmetry correlation structure to account for repeated measures within each subject. Standard residual diagnoses were used to check model assumptions. Log-transformations were used when needed. To $\log_{10}$-transform ddPCR values, 0 values were replaced with a small positive random number according to the detection limits. Logistic regression models were used to generate ROC curves. Optimal cutoff values were selected by treating sensitivity and specificity as equally important. SAS version 9.4 was used for all analyses. All P values are two-sided and reported without adjustment for multiple comparisons.

Reporting summary

Further information on research design is available in the Nature Portfolio Reporting Summary linked to this article.

Data availability

The datasets that support the findings of this study are available in Supplementary Data 1, 2 and 3. Positive and negative controls for ISH, IF and IHC are available in Supplementary Data 3. The sequencing data of SARS-CoV-2 isolated from Vero E6-TMPRSS2-T2A-ACE2 cell culture of thalamus of P38 have been deposited to GenBank (OP125352).

Code availability

The SAS code for statistical analysis has been deposited at https://github.com/niaid/COVID-19-Autopsy-SAS-Code. The bioinformatic pipeline for HT-SGS data analysis has been deposited at https://github.com/niaid/UMI-pacbio-pipeline.

35. Huang, N. et al. SARS-CoV-2 infection of the oral cavity and saliva. *Nat. Med.* **27**, 892–903 (2021).
36. Burbelo, P. D. et al. Sensitivity in detection of antibodies to nucleocapsid and spike proteins of severe acute respiratory syndrome coronavirus 2 in patients with coronavirus disease 2019. *J. Infect. Dis.* **222**, 206–213 (2020).
37. Burbelo, P. D., Goldman, R. & Mattson, T. L. A simplified immunoprecipitation method for quantitatively measuring antibody responses in clinical sera samples by using mammalian-produced *Renilla* luciferase-antigen fusion proteins. *BMC Biotechnol.* **5**, 22 (2005).

38. Wölfel, R. et al. Virological assessment of hospitalized patients with COVID-19. *Nature* **581**, 465–469 (2020).
39. Corman, V. M. et al. Detection of 2019 novel coronavirus (2019-nCoV) by real-time RT-PCR. *Euro Surveill.* **25**, 2000045 (2020).
40. Martin, M. Cutadapt removes adapter sequences from high-throughput sequence reads. *EMBnet J.* **17**, 10–12 (2011).
41. Langmead, B. & Salzberg, S. L. Fast gapped-read alignment with Bowtie 2. *Nat. Methods* **9**, 357–359 (2012).
42. Carossino, M. et al. Detection of SARS-CoV-2 by RNAscope® in situ hybridization and immunohistochemistry techniques. *Arch. Virol.* **165**, 2373–2377 (2020).
43. Williamson, B. N. et al. Clinical benefit of Remdesivir in rhesus macaques infected with SARS-CoV-2. *Nature* **585**, 273–276 (2020).
44. Munster, V. J. et al. Respiratory disease in rhesus macaques inoculated with SARS-CoV-2. *Nature* **585**, 268–272 (2020).
45. Rosenke, K. et al. Hydroxychloroquine prophylaxis and treatment is ineffective in macaque and hamster SARS-CoV-2 disease models. *JCI Insight* **5**, e143174 (2020).

Acknowledgements This study was financed and supported by the Intramural Research Program of the National Institutes of Health, Clinical Center, the Center for Cancer Research within the National Cancer Institute, the National Institute of Dental and Craniofacial Research and the National Institute of Allergy and Infectious Diseases. This research was made possible through the National Institutes of Health (NIH) Medical Research Scholars Program, a public–private partnership supported jointly by the NIH and contributions to the Foundation for the NIH from the Doris Duke Charitable Foundation, Genentech, the American Association for Dental Research and the Colgate-Palmolive Company. The following reagent was obtained through BEI Resources, National Institute of Allergy and Infectious Diseases, NIH: *Cercopithecus aethiops* kidney epithelial cells expressing transmembrane protease, serine 2 and human angiotensin-converting Enzyme 2 (Vero E6-TMPRSS2-T2A-ACE2), NR-54970. We thank C. Martens, S. Anzick and K. Barbian for whole-genome sequencing and related analysis.

Author contributions D.S.C., K.M.V., S.R.S., M.J.R.-B., A.L.B., L.J.P.V., A.G., D.L.H., S.M.H. and D.E.K. contributed to the study design and protocols for autopsy procurement. A.P.P., J.M.D., M.E.R., A.G., N.H., M.P., S. Singireddy, J.W., K.R., R.C., J.E.C., A.J.B., K.A.B., A.M.W., P.A.M., M.A.N.M., E.E.K., M.M.S., K.K.S., D.L.H., T.M.S., D.T., R.J.M., S. Dahi, K.B.D., E.M.K., J.R., J.A.H., A.T., E.S.H., C.R.C., A.R.L., J.E.R., J.E., A.P.B., M.A.M., R.H.C., Z.A.C., M. Abdulmahdi, S. Sopha, T.G., S. Soherwardi, Y.S., M.T.M., K.S., D.B., B.R., M. Arnouk, J.W.E., R.P. and A.D.H. provided care for, recruited, collected samples from and/or procured medical records for the patients in this study. T.P., G.D., M.G.-C., E.S. and P.P. designed and produced the box used to safely collect CNS samples during autopsy. D.E.K., S.M.H., M.Q., W.J.Y., S.P.Y., B.G., M.S.D.M., S. Desar, S.T., N.N., X.J., S.R., E.D., N.O., K.Y., J.-Y.C., S.P. and G.S. conducted the autopsies and/or histological analysis. S.R.S., M.J.R.-B., A.P.P., J.M.D., A.L.B., L.J.P.V., S.C.R., S.J.C., E.R.E., B.L.K., J.A.O., M.B. and R.A.S. assisted with procurement and preservation of autopsy specimens. S.R.S. with assistance from S.C.R., J.M.D., A.P.P. and I.A.L. carried out RNA extraction, ddPCR and data analysis. M.S., C.K.Y., V.J.M. and E.d.W. carried out and analysed data for subgenomic RNA RT–PCR. C.W.W. and K.E.P. carried out IF. K.Y., J.-Y.C., S.C.R. and S.M.H. carried out ISH and chromogenic IHC. P.D.B. and J.I.C. measured antibody responses to SARS-CoV-2 in perimortem plasma samples. S.H.K., F.B. and E.A.B. carried out viral sequencing. J.S. carried out all statistical analyses. S.R.S. drafted the manuscript with critical input from D.S.C., K.M.V., S.M.H., D.E.K., S.C.R., A.P.P., M.J.R.-B., E.d.W., V.J.M., A.G., D.L.H., K.K.S., M.M.S., M.T.M., P.D.B., J.I.C., C.W.W., K.E.P. and S.J.C. All authors approved the submitted version of the manuscript.

Competing interests The authors declare no competing interests.

Additional information

Supplementary information The online version contains supplementary material available at https://doi.org/10.1038/s41586-022-05542-y.

Correspondence and requests for materials should be addressed to Daniel S. Chertow.

Peer review information *Nature* thanks the anonymous reviewers for their contribution to the peer review of this work. Peer reviewer reports are available.

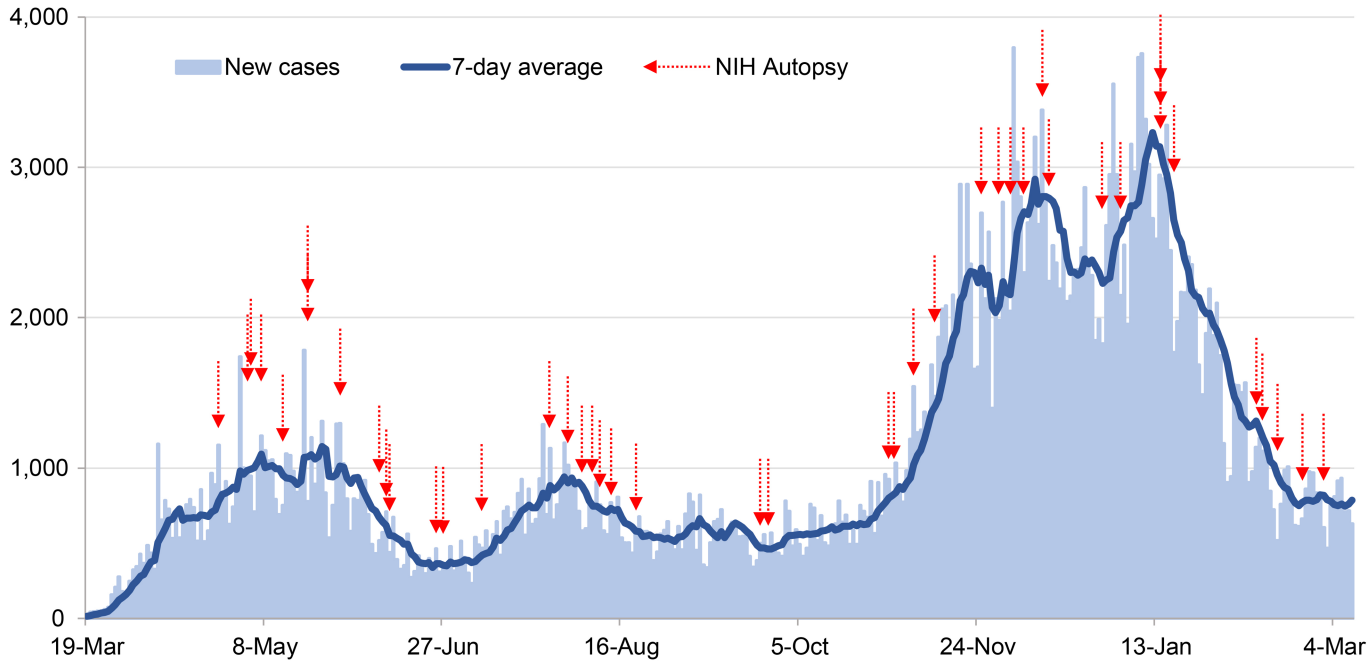

Extended Data Fig. 1 | Autopsy procurement relative to Maryland COVID-19 cases, March 19th, 2020 to March 9th, 2021. Daily COVID-19 reported cases for Maryland (light blue bars) with 7-day average (dark blue line) with timing of autopsies (red arrows).

a

Estimated difference log_{10} ddPCR (N copes/ng RNA): Resp vs Non-Resp		SE	p-value
Early	2.04	0.10	$3x10^{-22}$
Mid	1.36	0.12	$3x10^{-14}$
Late	0.67	0.11	$3x10^{-7}$

b

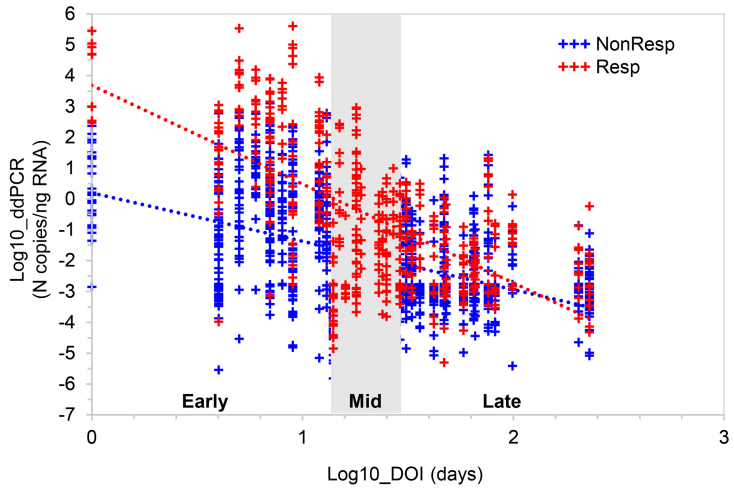

c

	Tissue Group	Intercept log_{10}ddPCR (N copies/ng RNA)	SE	Slope	SE	p-value
Respiratory	**All Respiratory**	**3.54**	**0.54**	**-3.14**	**0.39**	**$1x10^{-15}$**
	Nasopharynx	3.80	1.11	-2.64	0.76	0.0006
	Oropharynx	0.44	0.79	-1.79	0.56	0.0020
	Lower airway	3.13	0.70	-3.01	0.51	$5x10^{-9}$
	Lung parenchyma	4.48	0.69	-3.45	0.50	$2x10^{-11}$
Non-Respiratory	**All Non-Respiratory**	**0.16**	**0.52**	**-1.62**	**0.38**	**$2x10^{-5}$**
	Vasculature	1.20	0.56	-2.25	0.41	$5x10^{-8}$
	Myocardium	1.02	0.54	-2.12	0.39	$7x10^{-8}$
	Pericardium	2.60	0.68	-3.17	0.49	$2x10^{-10}$
	LN from head/neck	1.03	1.14	-1.92	0.80	0.0200
	LN from thorax	1.30	0.62	-1.56	0.44	0.0004
	LN from abdomen	-1.06	0.70	-0.87	0.54	0.1100
	Spleen	-0.15	0.66	-1.62	0.48	0.0008
	Intestines	-0.77	0.53	-1.29	0.38	0.0007
	Liver	-0.29	0.66	-1.66	0.48	0.0006
	Pancreas	-0.37	0.66	-1.45	0.48	0.0030
	Genitourinary	-0.65	0.54	-1.22	0.39	0.0020
	Endocrine	0.27	0.55	-1.81	0.40	$6x10^{-6}$
	Skeletal Muscle	0.83	0.64	-1.96	0.46	$2x10^{-5}$
	Other	0.05	0.76	-1.76	0.52	0.0007
	PNS	0.46	0.66	-1.47	0.47	0.0020
	Ocular Tissue	0.63	0.53	-1.97	0.38	$3x10^{-7}$
	CNS	-0.84	0.57	-0.66	0.40	0.1000

d

	Spearman correlation	95% CI	N
All jointly tested tissues	0.76	(0.73, 0.78)	1025
Early	0.88	(0.85, 0.89)	496
Mid	0.56	(0.47, 0.64)	253
Late	0.32	(0.21, 0.42)	276
Non-Resp	0.67	(0.63, 0.71)	656
Resp	0.86	(0.84, 0.89)	369

e

	Spearman correlation	95% CI	N
All jointly tested tissues	0.91	(0.88, 0.93)	302
Early	0.92	(0.90, 0.94)	250
Mid	0.84	(0.70, 0.91)	35
Late	0.65	(0.24, 0.86)	17
Non-Resp	0.80	(0.74, 0.85)	154
Resp	0.93	(0.91, 0.95)	148

f

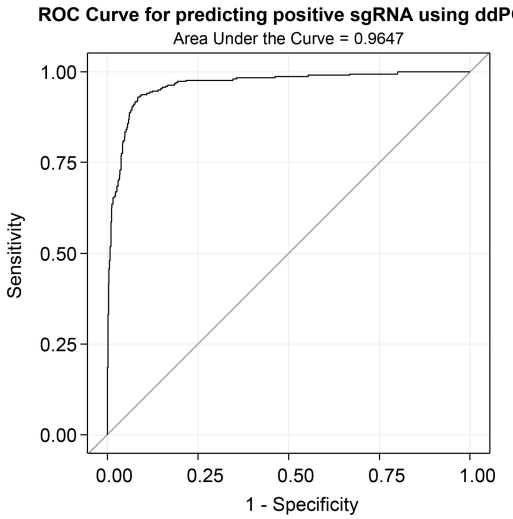

Extended Data Fig. 2 | Analysis of ddPCR quantification. (a) Linear mixed model analysis of estimated difference in log10ddPCR SARS-CoV-2 N copies/ng RNA between all respiratory and all non-respiratory tissues among early, mid, and late cases with SE and p-values from relevant contrasts, (b) graph of linear mixed model analysis comparing linear trends of log10ddPCR SARS-CoV-2 N copies/ng RNA by log10DOI of respiratory and non-respiratory tissues, (c) linear mixed model analysis estimating the linear trends of log10ddPCR SARS-CoV-2 N copies/ng RNA by log10DOI of individual tissue groups with intercept with standard error (SE), and slope with SE and p-values from relevant contrasts (a signification p-value indicates a non-zero slope), (d) Spearman correlation between ddPCR (N copies/ng RNA) and sgRNA (copies/µL RNA) for all tissues tested for sgRNA, with subset analyses of these tissues from early, mid and late cases and all non-respiratory and respiratory samples with 95% confidence intervals (CI), (e) Spearman correlation between ddPCR (N copies/ng RNA) and sgRNA (copies/µL RNA) for tissues jointly positive by both assays, with subset analyses of these tissues from early, mid, and late cases and all non-respiratory and respiratory samples with 95% CI, (f) receiver operating characteristic (ROC) curve of logistic regression using log10ddPCR in tissues to predict the detection of sgRNA in tissues, area under the curve is 0.965 (95% CI 0.953, 0.977), optimal cut-off for ddPCR is 1.47 N copies/ng RNA (sensitivity 93.0%, specificity 91.6%). All p-values were two-sided without adjustment for multiple comparisons.

a

	Patient	DOI (days)	Tissue	sgRNA (RNA*later*) Cq	sgRNA (RNA*later*) Copies/µL RNA	CPE	sgRNA (Flash Frozen) Tissue homogenate Cq	sgRNA (Flash Frozen) Cell culture supernatant Cq
Cq 15 to <20 n = 11	P37	5	Nasal Placode	15.96	1,592,517.55	+	23.57	17.84
	P18	9	R Superior Lobe	16.20	1,038,562.68	+	21.81	20.76
	P27	1	L Inferior Lobe	16.56	941,521.52	+	27.06	18.36
	P18	9	R Middle Lobe	16.68	751,163.28	+	21.45	19.11
	P27	1	L Superior Lobe	16.74	840,216.22	+	24.05	19.88
	P27	1	R Superior Lobe	17.55	605,097.14	+	25.54	19.03
	P18	9	L Inferior Lobe	17.61	399,355.23	+	26.07	19.15
	P18	9	R Inferior Lobe	18.28	252,263.17	+	21.96	19.59
	P24	12	R Middle Lobe	19.55	176,024.58	+	27.14	19.50
	P24	12	R Inferior Lobe	19.56	175,035.32	+	26.07	18.62
	P27	1	R Inferior Lobe	19.79	119,393.37	+	24.64	19.44
Cq 20 to <25 n = 14	P16	8	R Middle Lobe	20.52	140,774.62	+	29.87	18.68
	P19	7	Distal Trachea	20.61	51,758.95	+	23.91	21.58
	P37	5	Sinus Turbinate	21.02	51,430.26	+	29.88	18.33
	P32	6	L Bronchus	21.44	42,994.30	+	31.91	13.80
	P7	7	R Superior Lobe	21.52	30,890.52	+	27.27	17.93
	P32	6	Proximal Trachea	22.08	26,122.49	+	29.75	17.85
	P16	8	R Bronchus	22.42	25,076.22	+	33.77	17.39
	P22	4	R Middle Lobe	22.65	14,095.29	-	30.18	--
	P24	12	L Bronchus	23.68	10,796.93	-	--	--
	P38	13	L Inferior Lobe	23.69	6,419.78	-	35.09	--
	P36	4	L Inferior Lobe	24.03	5,030.85	+	34.08	19.28
	P43	18	Sinus Turbinate	24.29	6,828.27	-	30.83	--
	P22	4	R Superior Lobe	24.31	4,449.02	-	37.05	--
	P7	7	R Inferior Lobe	24.42	4,147.43	+	33.22	16.94
Cq 25 to <30 n = 16	P38	13	Thalamus	25.25	2,474.15	-	--	--
	P32	6	Choroid/Sclera	25.31	1,871.99	+	--	17.44
	P35	25	Skeletal Muscle	25.59	1,598.27	-	--	--
	P38	13	Hypothalamus	25.68	1,821.09	-	--	--
	P37	5	Thyroid	26.50	863.87	-	31.58	--
	P27	1	Pericardium	26.68	1,449.89	-	35.98	--
	P18	9	Abdominal Aorta	27.26	566.91	-	--	--
	P32	6	Liver	27.40	422.10	-	34.25	--
	P32	6	Jejunum	27.44	416.89	+	32.94	14.73
	P19	7	Mediastinal LN	27.96	353.22	+	--	16.29
	P27	1	R Ventricle	28.04	608.73	+	--	15.26
	P32	6	Thyroid	28.51	196.07	-	35.10	--
	P37	5	Optic Nerve	28.63	219.51	-	32.68	--
	P33	76	L Inferior Lobe	28.92	137.49	-	--	--
	P32	6	R Adrenal Gland	29.41	104.26	+	34.60	16.01
	P33	76	Thoracic LN	29.72	83.96	-	--	--
Cq 30 to <35 n =14	P21	12	R Inferior Lobe	31.21	41.88	-	--	--
	P36	4	Dura Mater	31.40	22.15	-	--	--
	P30	15	L Superior Lobe	31.41	17.77	-	--	--
	P32	6	Pancreas	31.56	23.03	-	--	--
	P28	7	R Inferior Lobe	31.75	20.42	-	--	--
	P38	13	Midbrain	31.94	20.39	-	--	--
	P38	13	Cervical Spinal Cord	32.12	17.97	-	--	--
	P33	76	R Kidney	32.29	13.74	-	--	--
	P6	19	L Inferior Lobe	32.49	16.19	-	--	--
	P28	7	Thoracic Aorta	33.30	6.63	-	--	--
	P40	47	Sciatic Nerve	33.41	6.47	-	--	--
	P22	4	Mediastinal LN	33.79	6.95	-	34.89	--
	P35	25	Uterus	33.99	3.29	-	--	--
	P25	9	L Inferior Lobe	34.51	5.38	-	--	--

b

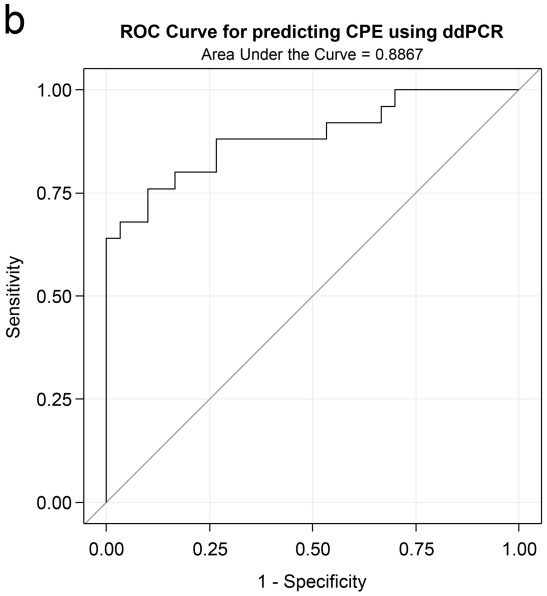

c

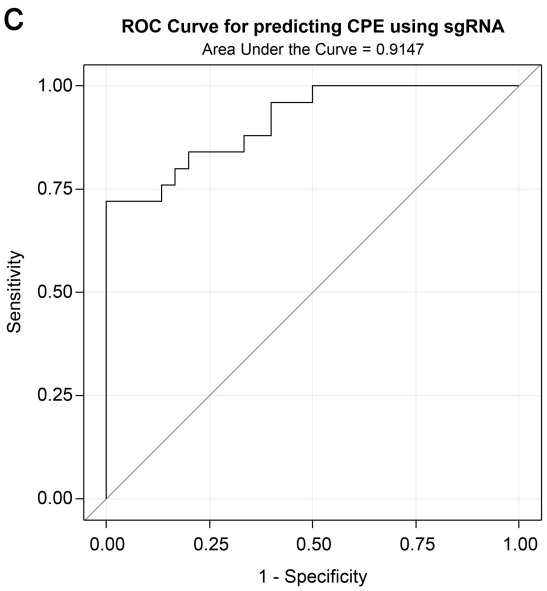

Extended Data Fig. 3 | Virus isolation summary and correlation between ddPCR and sgRNA. (a) Summary of 55 tissues selected for virus isolation organized by the sgRNA qPCR quantification cycle (Cq) for the RNA*later* preserved tissue, (b) Receiver operating characteristic (ROC) curve of logistic regression using $\log_{10}$ddPCR to predict the presence of cytopathic effect (CPE), area under the curve 0.887 (95% CI 0.795, 0.978), optimal cut-off for ddPCR is 758 N copies/ng RNA (sensitivity 76%, specificity 90%), (c) ROC curve of logistic regression using $\log_{10}$sgRNA to predict presence of CPE, area under the curve 0.915 (95% CI 0.843, 0.987), optimal cut-off for sgRNA is 25,069 copies/µL RNA (sensitivity 72%, specificity 100%). sgRNA qPCR was additionally performed on the flash frozen tissue homogenate and the supernatant from the least diluted tissue culture wells with CPE in order to rule out CPE from other causes; if both wells at that dilution showed CPE the samples were pooled.

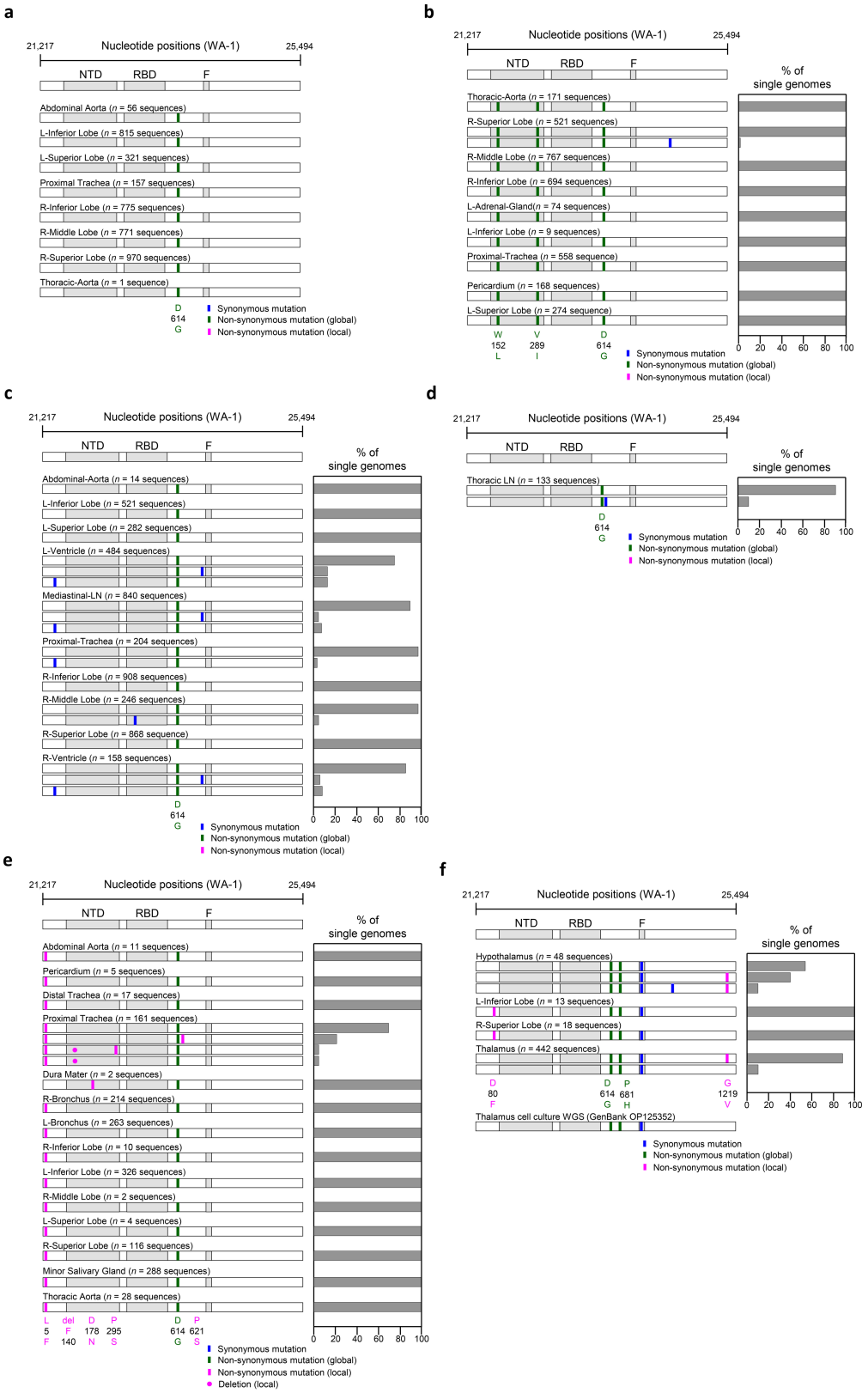

Extended Data Fig. 4 | Analysis of SARS-CoV-2 genetic diversity across body compartments in patients. (a) P18, (b) P19, (c) P27, (d) P33, (e) P36, (f) P38. Haplotype diagrams (left) show SARS-CoV-2 spike single genome sequences detected in multiple organs. Spike NH2-terminal domain (NTD), receptor-binding domain (RBD), and furin cleavage site (F) regions are shaded grey, and remaining regions of the spike are shaded white. Ticks with different colors indicate mutations relative to the WA-1 reference sequence; green indicates non-synonymous differences from WA-1 detected in all sequences in the individual; blue indicates synonymous mutations detected variably within the individual, and pink indicates non-synonymous mutations detected variably within the individual. Bar graphs (right) show the percentage of all single genome sequences in the sample matching each haplotype. The spike region of the consensus sequence generated from short read, whole genome sequencing (WGS) of the supernatant of P38 thalamus frozen tissue on Vero E6-TMPRSS2-T2A-ACE2 cells is additional shown at the bottom of (f) for comparison.

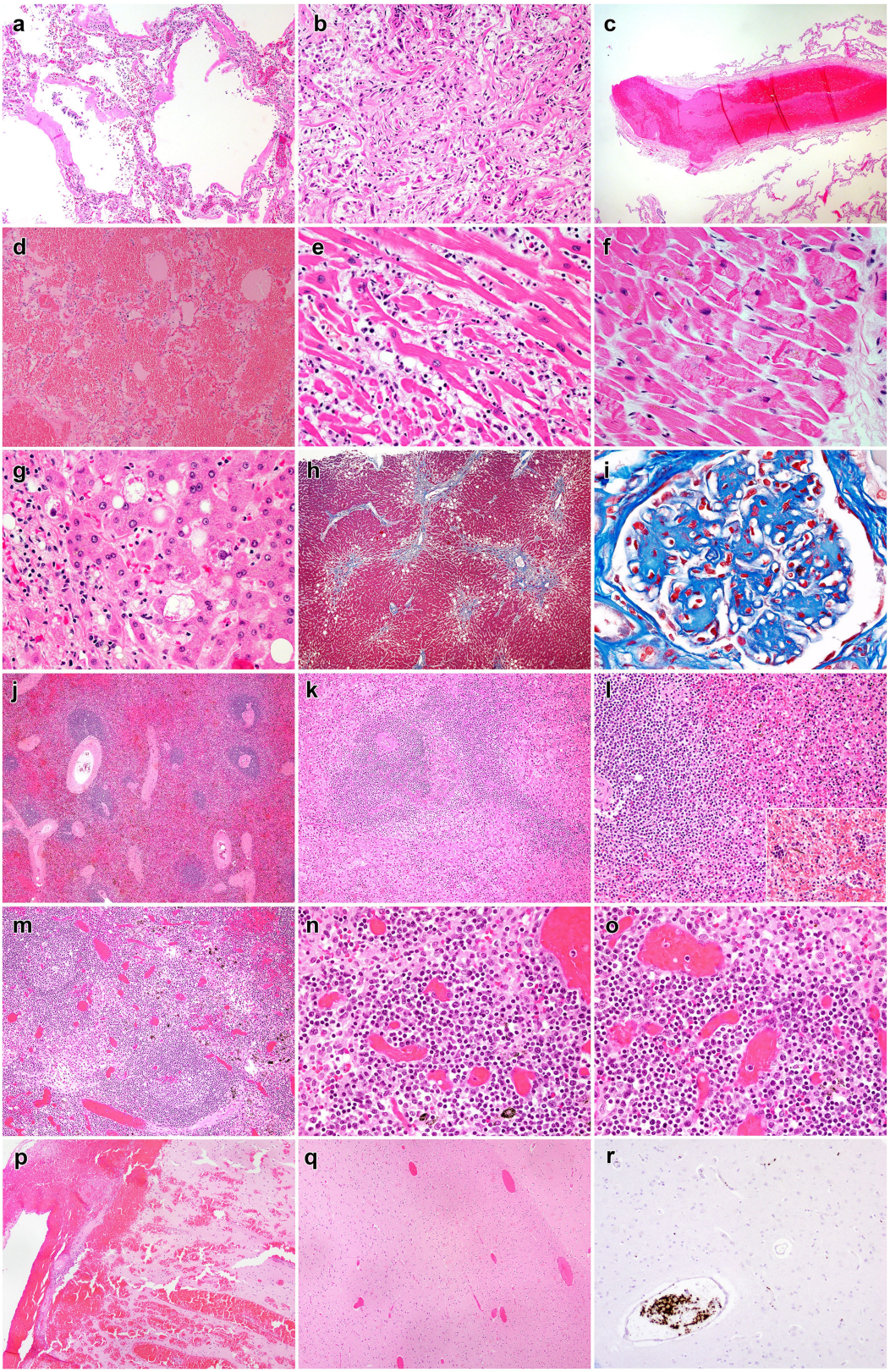

Extended Data Fig. 5 | See next page for caption.

Extended Data Fig. 5 | Representative histopathologic findings in COVID-19 autopsy patients. (a) Lung, Subject P22, exudative phase diffuse alveolar damage with hyaline membranes and mild interstitial inflammation (H&E, 100x), (b) Lung, Subject P26, proliferative phase diffuse alveolar damage and sparse inflammation (H&E, 200x), (c) Lung, Subject P22, organizing thrombus in medium sized pulmonary artery (H&E, 40x), (d) Lung, Subject P28. Diffuse pulmonary hemorrhage (H&E, 100x), (e) Heart, Subject P3, active lymphocytic myocarditis with cardiomyocyte necrosis (H&E, 400x), (f) Heart, Subject P38, microscopic focus of bland myocardial contraction band necrosis (H&E, 400x), (g) Liver, Subject P41, steatohepatitis with mild steatosis and scattered ballooned hepatocytes (H&E, 400x), (h) Liver, Subject P41, focal bridging fibrosis involving central hepatic veins (Masson trichrome, 40x), (i) Kidney, Subject P16, nodular glomerulosclerosis (Masson trichrome, 600x), (j) Spleen, Subject P16, preservation of white pulp and congestion (H&E, 40x), (k) Spleen, Subject P14, lymphoid depletion of white pulp with proteinaceous material and red pulp congestion (H&E, 100x), (l) Spleen, Subject P34, relative preservation of white pulp with extramedullary hematopoiesis (inset) in red pulp (H&E, 200x), (m) Lymph node, Subject P25, follicular hyperplasia with well-defined follicles (H&E), (n) Lymph node, Subject P25, marked plasmacytosis in the medullary cord (H&E, 400x), (o) Lymph node, Subject P25, marked plasmacytosis and sinus histiocytosis (H&E, 400x), (p) Brain, Subject P35, focal subarachnoid and intraparenchymal hemorrhage (H&E, 40x), (q) Brain, Subject P44, vascular congestion (H&E, 40x), (r) Brain, Subject P43, intravascular platelet aggregates (anti-CD61 stain, 100x). All H&E (and Masson trichrome) photomicrographs are exemplars of histopathology observed across a diversity of patients within the cohort, see Extended Data Table 4 for a summary of histopathology observed across the autopsy cohort and Supplemental data 2b for individual case-level data. The histopathologic observations were validated by a minimum of two board certified anatomic pathologist.

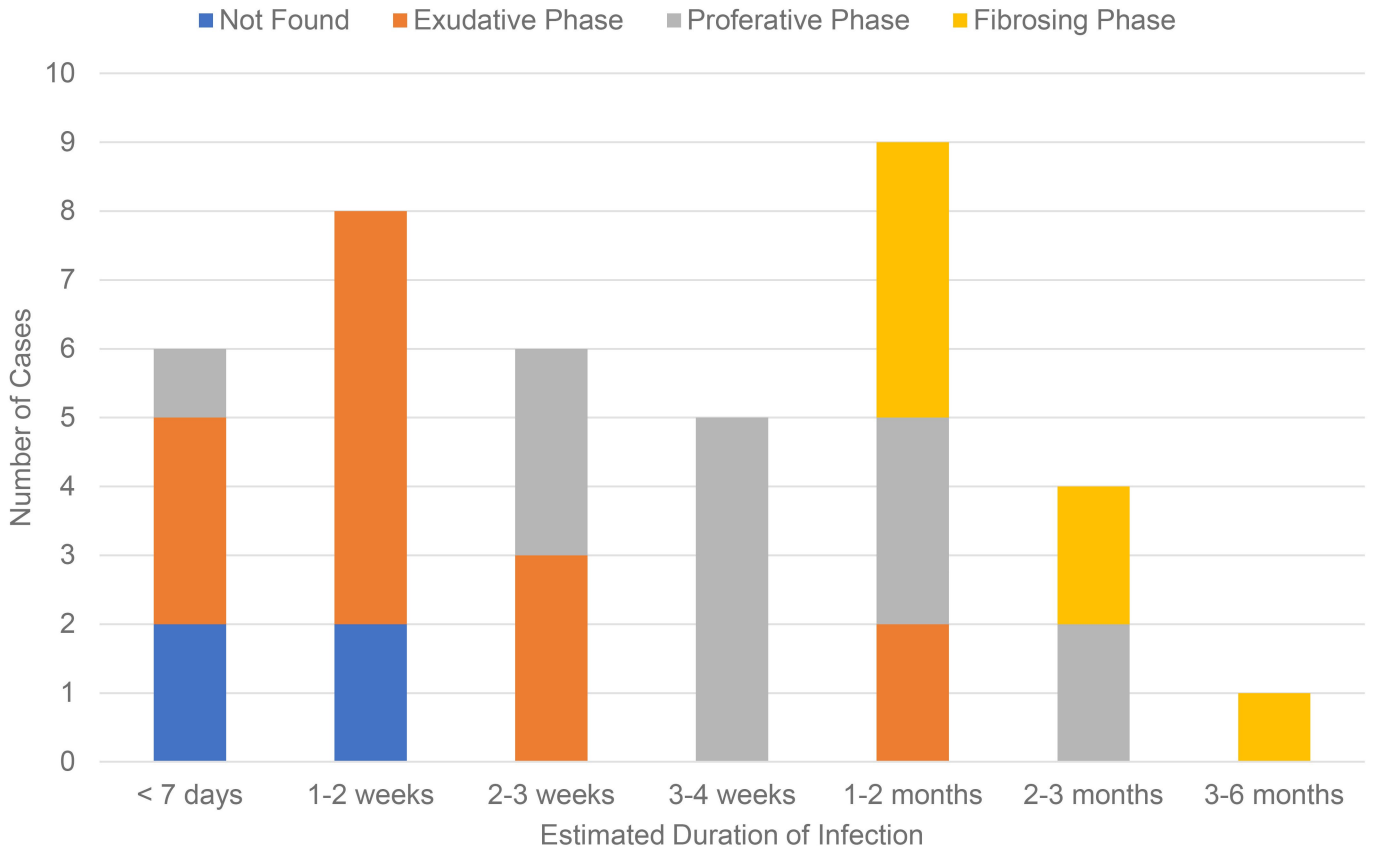

Extended Data Fig. 6 | Temporal association of diffuse alveolar damage in patients dying from COVID-19. Number of autopsy cases with diagnosed phase of diffuse alveolar damage (DAD) via histopathologic analysis by duration of illness. Early time points mainly show the initial exudative phase of diffuse alveolar damage, while patients dying after prolonged illness are more likely to have proliferative or fibrosing phases of DAD.

Extended Data Table 1 | Autopsy cohort demographics, comorbidities, and clinical intervention summary

a

Age (years)	**(n=44)**
Median (IQR)	62.5 (47.3-71.0)
Age by group (years)	**n (%)**
0-17	1 (2.3)
18-24	1 (2.3)
25-34	2 (4.5)
35-44	6 (13.6)
45-54	4 (9.1)
55-64	11 (25.0)
65-74	11 (25.0)
75-84	5 (11.4)
≥85	3 (6.8)
Sex	
Male	30 (68.2)
Female	13 (29.5)
Intersex	1 (2.3)
Race/Ethnicity	
Non-Hispanic Asian	1 (2.3)
Non-Hispanic Black or African American	18 (40.9)
Non-Hispanic White	18 (40.9)
Hispanic or Latino	7 (15.9)
Body mass index (BMI)	
<18.5	2 (4.5)
18.5-24.9	9 (20.5)
25-29.9	10 (22.7)
30-34.9	9 (20.5)
35.0-39.9	6 (13.6)
≥40	8 (18.1)
Comorbidities pre-COVID-19 diagnosis	
1+	43 (97.7)
2+	34 (77.3)
3+	27 (61.4)
Autoimmune disease	5 (11.4)
Cancer	7 (15.9)
Cardiovascular disease	15 (34.1)
Cerebrovascular disease	5 (11.4)
Chronic immunosuppression	4 (9.1)
Chronic respiratory disease	16 (36.4)
Diabetes mellitus	14 (31.8)
History of thromboembolic event(s)	4 (9.1)
Hypertension	27 (61.4)
Hyperlipidemia	14 (31.8)
Liver disease	3 (6.8)
Obesity (BMI ≥30)	23 (52.3)
Renal disease	8 (18.2)

b

Disease Course Intervals	**Median (IQR)**
Symptom onset to hospitalization*, days	6 (3-10)
Hospitalization* to death, days	12 (5.75-30.25)
Symptom onset to death, days	18.5 (11.25-37.5)
Postmortem interval, hr	22.2 (18.2-33.9)
Pharmacologic Interventions	**n (%)**
Vasopressors	38 (86.4)
Antibiotics	41 (93.2)
Paralytics	25 (56.8)
Systemic steroids	39 (88.6)
Systemic anticoagulation	34 (77.3)
Inhaled vasodilators	10 (22.7)
Remdesivir	16 (36.4)
Tocilizumab	4 (9.1)
Convalescent plasma	6 (13.6)
Nonpharmacologic Interventions	
Extracorporeal membrane oxygenation (ECMO)	10 (22.7)
Invasive mechanical ventilation (IMV)	34 (77.3)
Non-invasive ventilation (NIV)	4 (9.1)
Nasal Cannula	5 (11.4)
Tracheostomy	9 (20.5)
Chest tube(s)	11 (25.0)
Renal replacement therapy	18 (40.9)

(a) Summary of demographics and known comorbidities for autopsy cases, (b) Summary of illness course and clinical care for autopsy cases. Data compiled from available patient medical records. ECMO/extracorporeal membrane oxygenation. *In reference to final hospitalization prior to death if hospitalized multiple times following COVID-19 diagnosis. IQR/interquartile range.

Extended Data Table 2 | Summary of SARS-CoV-2 RNA and subgenomic RNA by tissue group over time

a

Tissue Group	DOI (days)	Median N gene copies/ ng RNA	Interquartile Range Q1	Q3
Nasopharynx	≤14	15,631.7545	0.2399	189,771.2393
	15-30	890.4679	851.2936	929.6422
	≥31	0.0484	0.0171	0.3285
Oropharynx	≤14	0.7074	0.1679	5.6633
	15-30	0.0052	0.0000	0.1855
	≥31	0.0000	0.0000	0.0060
Lower Airway	≤14	22.7900	0.3319	396.2547
	15-30	0.0261	0.0033	0.0741
	≥31	0.0088	0.0000	0.0389
Lung Parenchyma	≤14	246.8247	5.5016	1,821.3350
	15-30	0.2926	0.0147	1.9439
	≥31	0.0322	0.0035	0.2270
Vasculature	≤14	1.2451	0.0244	12.2114
	15-30	0.0000	0.0000	0.0336
	≥31	0.0000	0.0000	0.0099
Myocardium	≤14	1.0062	0.0000	14.7105
	15-30	0.0000	0.0000	0.0138
	≥31	0.0000	0.0000	0.0082
Pericardium	≤14	1.7073	0.2097	38.6329
	15-30	0.0000	0.0000	0.0404
	≥31	0.0000	0.0000	0.0037
LN from Head/Neck	≤14	3.9345	0.2294	5.9371
	15-30	0.0000	0.0000	0.0199
	≥31	0.0251	0.0018	0.1238
LN from Thorax	≤14	1.3989	0.0567	21.8166
	15-30	0.1041	0.0348	0.6487
	≥31	0.0779	0.0000	0.3470
LN from Abdomen	≤14	0.0181	0.0000	0.8165
	15-30	0.0000	0.0000	0.0203
	≥31	0.0000	0.0000	0.0000
Spleen	≤14	0.0420	0.0000	0.5095
	15-30	0.0000	0.0000	0.0000
	≥31	0.0000	0.0000	0.0000
Gastrointestinal	≤14	0.0144	0.0000	0.6235
	15-30	0.0000	0.0000	0.0091
	≥31	0.0000	0.0000	0.0000
Liver	≤14	0.0222	0.0000	0.4274
	15-30	0.0000	0.0000	0.0035
	≥31	0.0000	0.0000	0.0000
Pancreas	≤14	0.0354	0.0000	0.3606
	15-30	0.0000	0.0000	0.0069
	≥31	0.0000	0.0000	0.0000
Genitourinary	≤14	0.1998	0.0000	2.6556
	15-30	0.0000	0.0000	0.0249
	≥31	0.0000	0.0000	0.0035
Endocrine	≤14	0.0450	0.0000	0.3527
	15-30	0.0000	0.0000	0.0032
	≥31	0.0000	0.0000	0.0000
Skeletal Muscle	≤14	0.7588	0.0000	3.0667
	15-30	0.0150	0.0000	0.2074
	≥31	0.0000	0.0000	0.0038
Other	≤14	0.7091	0.0244	1.5590
	15-30	0.0000	0.0000	0.0000
	≥31	0.0000	0.0000	0.0000
Peripheral Nervous System	≤14	0.6275	0.0211	5.3350
	15-30	0.0024	0.0000	0.0347
	≥31	0.0449	0.0000	0.3336
Ocular	≤14	1.4388	0.0092	13.4383
	15-30	0.0000	0.0000	0.0307
	≥31	0.0000	0.0000	0.0045
Central Nervous System	≤14	0.1349	0.0112	2.3441
	15-30	0.0047	0.0000	1.4675
	≥31	0.0207	0.0035	0.3227

b

Tissue	DOI (days)	ddPCR+ (n, %)	sgRNA+ (n,%)
All Respiratory		**43/44, 99.7**	**24/43, 55.8**
Nasopharynx	≤14	2/2, 100	1/2, 50
	15-30	1/1, 100	1/1, 100
	≥31	2/2, 100	0/2 (0)
	Total	*5/5, 100*	*2/5, 20.0*
Oropharynx	≤14	8/11, 72.7	5/8, 62.5
	15-30	5/11, 45.5	2/5, 40.0
	≥31	4/13, 30.8	1/3, 33.3
	Total	*17/35, 48.6*	*8/16, 50.0*
Lower Airway	≤14	15/17, 88.2	12/15, 80.0
	15-30	11/13, 84.6	1/11, 9.1
	≥31	13/14, 92.9	1/13, 7.7
	Total	*39/44, 88.6*	*14/39, 35.9*
Lung Parenchyma	≤14	16/17, 94.1	14/16, 87.5
	15-30	13/13, 100	5/13, 38.5
	≥31	14/14, 100	3/14, 21.4
	Total	*43/44, 97.7*	*22/43, 51.2*
All Cardiovascular		**35/44, 79.5**	**14/35, 40**
Vasculature	≤14	13/14, 92.9	10/13, 76.9
	15-30	6/10, 60.0	2/6, 33.3
	≥31	7/14, 50.0	1/7, 14.3
	Total	*26/38, 68.4*	*13/26, 50.0*
Myocardium	≤14	14/17, 82.4	8/14, 57.1
	15-30	8/13, 61.5	0/8, 0
	≥31	9/14, 64.3	0/9, 0
	Total	*31/44, 70.5*	*8/31, 25.8*
Pericardium	≤14	15/17, 88.2	7/15, 46.7
	15-30	5/13, 38.5	1/5, 20.0
	≥31	4/13, 30.8	0/4, 0
	Total	*24/43, 55.8*	*8/24, 33.3*
All Lymphoid		**38/44, 86.4**	**15/38, 39.5**
LN from Head/Neck	≤14	4/5, 80.0	3/4, 75.0
	15-30	2/6, 33.3	0/2, 0
	≥31	6/8, 75	0/6, 0
	Total	*12/19, 63.2*	*3/12, 25.0*
LN from Thorax	≤14	15/17, 88.2	11/15, 73.3
	15-30	11/13, 84.6	2/11, 18.2
	≥31	12/13, 92.3	2/12, 16.7
	Total	*38/43, 88.4*	*15/38, 39.5*
LN from Abdomen	≤14	6/12, 50.0	2/6, 33.3
	15-30	4/9, 44.4	0/4, 0
	≥31	1/5, 20.0	0/1, 0
	Total	*11/26, 42.3*	*2/11, 18.2*
Spleen	≤14	12/17, 70.6	3/12, 25.0
	15-30	3/13, 23.1	0/3, 0
	≥31	2/14, 14.3	0/2, 0
	Total	*17/44, 38.6*	*3/17, 17.6*
All Gastrointestinal		**32/44, 72.7**	**8/32, 25.0**
Small Intestine	≤14	13/17, 76.5	2/13, 15.4
	15-30	7/13, 53.8	1/7, 14.3
	≥31	5/14, 35.7	0/5, 0
	Total	*25/44, 56.8*	*3/25, 12.0*
Large Intestine	≤14	12/17, 70.6	3/12, 25.0
	15-30	4/13, 30.8	0/4, 0
	≥31	3/14, 21.4	1/3, 33.3
	Total	*19/44, 43.2*	*4/19, 21.1*
Liver	≤14	10/17, 58.8	4/10, 40.0
	15-30	5/13, 38.5	0/5, 0
	≥31	3/14, 21.4	0/2*, 0
	Total	*18/44, 40.9*	*4/17, 23.5*
Pancreas	≤14	11/17, 64.7	3/11, 27.3
	15-30	3/12, 25.0	0/3, 0
	≥31	2/14, 14.3	0/2, 0
	Total	*16/43, 37.2*	*3/16, 18.8*
Genitourinary		**22/44, 50.0**	**7/22, 31.8**
Kidney	≤14	12/17, 70.6	4/12, 33.3
	15-30	5/13, 38.5	0/5, 0
	≥31	3/14, 21.4	1/3, 33.3
	Total	*20/44, 45.5*	*5/20, 25.0*
Testis	≤14	7/10, 70.0	1/7, 14.3
	15-30	1/8, 12.5	0/1, 0
	≥31	3/12, 25.0	0/3, 0
	Total	*11/30, 36.7*	*1/11, 9.1*
Ovary	≤14	3/5, 60.0	0/3, 0
	15-30	0/3, 0	NA
	≥31	NA	NA
	Total	*3/8, 37.5*	*0/3, 0*
Uterus	≤14	1/1, 100	0/1, 0
	15-30	2/2, 100	1/2, 50.0
	≥31	NA	NA
	Total	*3/3, 100*	*1/3, 33.3*

Tissue	DOI (days)	ddPCR+ (n, %)	sgRNA+ (n,%)
Endocrine		**23/44, 52.3**	**9/23, 39.1**
Adrenal Gland	≤14	12/16, 75.0	5/12, 41.7
	15-30	4/13, 30.8	0/4, 0
	≥31	5/14, 35.7	0/5, 0
	Total	*21/43, 48.8*	*5/21, 23.8*
Thyroid	≤14	10/16, 62.5	7/10, 70.0
	15-30	4/12, 33.3	0/4, 0
	≥31	3/13, 23.1	0/3, 0
	Total	*17/41, 41.5*	*7/17, 41.2*
Muscle, Skin, & Nerve		**30/44, 68.2**	**9/30, 30.0**
Psoas Muscle	≤14	12/17, 70.6	5/12, 41.7
	15-30	7/13, 53.8	1/7, 14.3
	≥31	3/14, 21.4	0/3, 0
	Total	*22/44, 50.0*	*6/22, 27.3*
Skin	≤14	3/3, 100	1/3, 33.3
	15-30	1/1, 100	0/1, 0
	≥31	1/7, 14.3	0/1, 0
	Total	*5/11, 45.5*	*1/5, 20.0*
Sciatic Nerve	≤14	13/15, 86.7	5/13, 38.5
	15-30	5/10, 50.0	0/5, 0
	≥31	7/14, 50.0	2/7, 28.6
	Total	*25/39, 64.1*	*7/25, 28.0*
Ocular		**22/38, 57.9**	**7/22, 31.8**
Ocular Tissue	≤14	9/12, 75.0	6/9, 66.7
	15-30	4/9, 44.4	0/4, 0
	≥31	6/11, 54.5	1/5*, 20.0
	Total	*19/32, 59.4*	*7/18, 38.9*
Optic Nerve	≤14	10/12, 83.3	3/10, 30.0
	15-30	2/6, 33.3	0/2, 0
	≥31	5/11, 45.5	0/5, 0
	Total	*17/29, 58.6*	*3/17, 17.6*
Central Nervous System		**10/11, 90.9**	**4/10, 40.0**
Cervical Spinal Cord	≤14	2/2, 100	1/2, 50.0
	15-30	1/1, 100	0/1, 0
	≥31	5/6, 83.3	0/5, 0
	Total	*8/9, 88.9*	*1/8, 12.5*
Olfactory Nerve	≤14	2/3, 66.7	1/2, 50.0
	15-30	1/2, 50.0	0/1, 0
	≥31	3/5, 60.0	0/3, 0
	Total	*6/10, 60.0*	*1/6, 16.7*
Basal Ganglia	≤14	1/2, 50.0	0/1, 0
	15-30	1/2, 50.0	0/1, 0
	≥31	3/4, 75.0	0/3, 0
	Total	*5/8, 62.5*	*0/5, 0*
Cerebral Cortex	≤14	3/3, 100	1/3, 33.3
	15-30	1/2, 50.0	1/1, 100
	≥31	5/6, 83.3	0/5, 0
	Total	*9/11, 81.8*	*2/9, 22.2*
Brainstem	≤14	3/3, 100	1/3, 33.3
	15-30	1/2, 50.0	1/1, 100
	≥31	4/5, 80.0	0/4, 0
	Total	*8/10, 80.0*	*2/8, 25.0*
Cerebellum	≤14	2/3, 66.7	0/2, 0
	15-30	1/2, 50.0	0/1, 0
	≥31	6/6, 100	0/6, 0
	Total	*9/11, 81.8*	*0/9, 0*
Thalamus	≤14	2/2, 100	1/2, 50.0
	15-30	1/2, 50.0	0/1, 0
	≥31	5/6, 83.3	0/5, 0
	Total	*8/10, 80.0*	*1/8, 12.5*
Hypothalamus	≤14	2/2, 100	1/2, 50.0
	15-30	1/1, 100	0/1, 0
	≥31	4/4, 100	0/4, 0
	Total	*7/7, 100*	*1/7, 14.3*
Corpus Callosum	≤14	2/2, 100	0/2, 0
	15-30	1/1, 100	0/1, 0
	≥31	4/4, 100	0/4, 0
	Total	*7/7, 100*	*0/7, 0*
Dura Mater	≤14	3/3, 100	2/3, 66.7
	15-30	0/1, 0	NA
	≥31	0/5, 0	NA
	Total	*3/9, 33.3*	*2/3, 66.7*
Fluids		**17/43, 39.5**	**3/17, 17.6**
Perimortem Plasma	≤14	11/16, 68.8	2/11, 18.2
	15-30	1/11, 9.1	0/1, 0
	≥31	0/14, 0	NA
	Total	*12/41, 29.3*	*2/12, 16.7*
Ocular Humors	≤14	6/14, 42.9	1/6, 16.7
	15-30	3/11, 27.3	0/3, 0
	≥31	2/10, 20.0	0/1*, 0
	Total	*11/35, 31.4*	*1//11, 9.1*

(a). Summary of the median and interquartile range of Nucleocapsid gene copies/ng RNA across by tissue group and duration of illness (days), (b) summary of the number and percentage of cases with SARS-CoV-2 RNA detected via droplet digital (dd)PCR by tissue group for all cases and by tissue and duration of illness (days). The number and percentage of tissues positive for ddPCR that were additionally positive for subgenomic (sg)RNA PCR is listed in the right most column. *A tissue positive via ddPCR was not tested via subgenomic RNA PCR. CNS/central nervous system, LN/lymph node.

Extended Data Table 3 | SARS-CoV-2 cellular tropism

SARS-CoV-2 cellular tropism demonstrated by *in situ* hybridization				
Tissue	Cell type(s)	Associated panel(s)		
		Fig. 2	Fig. 3	Supplementary Data 3
Sinus turbinate	Mucus secreting epithelium			a
Lip	Squamous epithelium, minor salivary gland			b, c
Trachea	Endothelium, smooth muscle, chondrocyte			k, gg
Bronchus	Bronchial epithelium, endothelium, mucus secreting epithelium, smooth muscle			d, e, jj
Lung	Pneumocytes (Type I & II), hyaline membrane, mononuclear leukocyte			f, g
Aorta	Tunica intima, tunica media			i, j
Heart	Cardiac myocyte			h
Pericardium	Fibroblast			ii
Lymph node	Mononuclear leukocytes			bb, cc
Spleen	Mononuclear leukocytes	c		dd
Esophagus	Stratified squamous epithelium	b		l
Ileum	Intestinal epithelium, smooth muscle			ff
Appendix	Colonic epithelium, mononuclear leukocytes	d		m
Colon	Colonic epithelium, mononuclear leukocytes			n
Liver	Hepatocytes, bile duct epithelium, Kupffer cells			o, p
Pancreas	Exocrine pancreatic cells, arterial smooth muscle			q, ee
Kidney	Glomerular epithelium, tubular epithelium			t, u
Testis	Sertoli cells, maturing germ cells, spermatid, Leydig cells, seminiferous tubule epithelium	g		y, z, aa
Ovary	Stromal cells	f		x
Uterus	Endometrial gland epithelium, stroma, myometrium	h		v, w
Adrenal gland	Endocrine secretory cells, adrenal cortical epithelium	e		r
Thyroid	Follicular cells	a		s
Psoas muscle	Skeletal muscle			kk
Skin	Epithelium, outer root sheath of hair follicle			hh
Sciatic nerve	Schwann cells			ll
Cervical spinal cord	Ependymal cells, NOS (white matter)		h,i	vv, xx
Basal ganglia	NOS		n,o	ss
Frontal lobe	NOS			mm
Parietal lobe	NOS			nn
Temporal lobe	NOS			ww
Occipital lobe	Endothelium, NOS			oo
Midbrain	NOS			tt
Cerebellum	Neurons within granular layer		k,l	uu
Thalamus	NOS			qq
Hypothalamus	NOS		b,c	rr
Corpus Callosum	NOS			pp

Summary of tissues with cell types that were identified as SARS-CoV-2 positive by *in situ* hybridization (ISH) with the associated panels demonstrating the cellular tropism within Fig. 2, Fig. 3, and Supplementary Data 3. NOS/not otherwise specified.

Extended Data Table 4 | Histopathologic findings of COVID-19 autopsy cases

Cause of Death	**N = 44**
Death with (but not from) COVID-19	6 (14%)
Death from COVID-19 or complications	38 (86%)
Pulmonary Findings[1]	**N (%) or Median (IQR)**
Left Lung Weight (g)[2]	795 (327)
Right Lung Weight (g)[2]	820 (365)
Combined Lung Weight (g)	1600 (528)
Diffuse Alveolar Damage	
Exudative	14 (32%)
Proliferate	15 (34%)
Fibrosing	7 (16%)
Not Found	8 (18%)
Acute Pneumonia	27 (61%)
Pulmonary Edema	30 (68%)
Pulmonary Hemorrhage (at least focal)	14 (32%)
Pulmonary Thromboembolism, Infarction	10 (23%)
Emphysematous changes (underlying COPD)	12 (27%)
Cardiac Findings	
Heart Weight (g)	500 (175)
Myocardial Infiltrate	4 (9%)
Focal infiltrate without myocyte necrosis	3 (7%)
Diffuse lymphocytic myocarditis	1 (2%)
Myocardial Ischemic Necrosis	
Remote, fibrotic	5 (11%)
Acute microscopic ischemia	4 (9%)
Coronary Artery Disease with ≥ 50% in at least 1 artery	16 (36%)
Renal Findings	
Left Kidney Weight (g)[4]	180 (107)
Right Kidney Weight (g)[4]	168 (79)
Changes consistent with Acute Kidney Injury	17 (39%)
Changes consistent with Diabetic glomerulopathy	10 (23%)
Splenic Findings	
Splenic Weight (g)	235 (215)
Follicular hyperplasia	15 (34%)
Lymphodepletion	
Present	8 (18%)
Some, Partial Preservation	34 (77%)
No Lymphodepletion	2 (5%)
Red Pulp Congestion	35 (80%)
Infarction	2 (5%)

Lymph Node Findings[5]	**N (%) or Median (IQR)**
Lymphodepletion	
Present	5 (12%)
Some, Partial Preservation	4 (10%)
No Lymphodepletion	31 (78%)
Follicular Hyperplasia	
Present	22 (55%)
Present, regressed	2 (5%)
Paracortical Hyperplasia	32 (80%)
Plasmacytosis	19 (48%)
Plasmablasts noted	4 (10%)
Hepatic Findings[3]	
Liver Weight (g)[4]	1670 (900)
Hepatic necrosis	
None	30 (70%)
Zonal	12 (28%)
% Zonal Necrosis	30% (40%)
Massive	1 (2%)
Steatosis	
None to Minimal	24 (56%)
Mild	14 (33%)
Moderate	5 (12%)
Steatohepatitis	5 (12%)
Portal Inflammation	
None to Minimal	16 (37%)
Mild	23 (53%)
Moderate	4 (9%)
Fibrosis	
None	27 (63%)
Periportal or perisinusoidal	6 (14%)
Periportal and perisinusoidal	1 (2%)
Bridging fibrosis	6 (14%)
Cirrhosis	3 (7%)
Central Nervous System Findings (N=11)	
Brain Weight (g)	1350 (230)
Hypoxic/Ischemic Injury (focal or diffuse)	5 (45%)
Vascular congestion	5 (45%)
Focal (microscopic) hemorrhage	2 (18%)
No pathological findings	3 (27%)

Summary of histopathologic findings across organ system across 44 autopsy cases. Central nervous system findings are reported for the 11 cases in which consent for sampling was obtained. [1]Includes one case in which the COVID lungs were transplanted and data from explanted lungs used in table. [2]Individual lung weights were missing in 4 cases. [3]Findings missing on 1 case due to extreme autolysis. [4]Weight missing on one case. [5]Lymph node findings missing in 4 cases.

nature portfolio

Corresponding author(s): Daniel S. Chertow

Last updated by author(s): Sep 29, 2022

Reporting Summary

Nature Portfolio wishes to improve the reproducibility of the work that we publish. This form provides structure for consistency and transparency in reporting. For further information on Nature Portfolio policies, see our Editorial Policies and the Editorial Policy Checklist.

Statistics

For all statistical analyses, confirm that the following items are present in the figure legend, table legend, main text, or Methods section.

n/a	Confirmed
☐	☒ The exact sample size (*n*) for each experimental group/condition, given as a discrete number and unit of measurement
☐	☒ A statement on whether measurements were taken from distinct samples or whether the same sample was measured repeatedly
☐	☒ The statistical test(s) used AND whether they are one- or two-sided *Only common tests should be described solely by name; describe more complex techniques in the Methods section.*
☐	☒ A description of all covariates tested
☐	☒ A description of any assumptions or corrections, such as tests of normality and adjustment for multiple comparisons
☐	☒ A full description of the statistical parameters including central tendency (e.g. means) or other basic estimates (e.g. regression coefficient) AND variation (e.g. standard deviation) or associated estimates of uncertainty (e.g. confidence intervals)
☐	☒ For null hypothesis testing, the test statistic (e.g. *F*, *t*, *r*) with confidence intervals, effect sizes, degrees of freedom and *P* value noted *Give P values as exact values whenever suitable.*
☒	☐ For Bayesian analysis, information on the choice of priors and Markov chain Monte Carlo settings
☒	☐ For hierarchical and complex designs, identification of the appropriate level for tests and full reporting of outcomes
☐	☒ Estimates of effect sizes (e.g. Cohen's *d*, Pearson's *r*), indicating how they were calculated

Our web collection on statistics for biologists contains articles on many of the points above.

Software and code

Policy information about availability of computer code

Data collection	ddPCR raw data was collected using QuantaSoft version 1.7.4.0917 (Bio-Rad).
Data analysis	ddPCR raw data was analyzed using QuantaSoft Analysis Pro version 1.0.596 (Bio-Rad). HT-SGS data analysis is described in detail in PMID 33831133; the bioinformatic pipeline for HT-SGS data analysis has been deposited (https://github.com/niaid/UMI-pacbio-pipeline) Raw sequence reads from the P38 thalamus isolated virus were trimmed of Illumina adapter sequence using Cutadapt version 1.1241 and then trimmed and filtered for quality using the fastq_quality_trimmer and fastq_quality_filter tools from the FASTX-Toolkit 0.0.14 (Hannon Lab, CSHL);reads were mapped to the SARS-CoV-2 2019-nCoV/USA-WA1/2020 genome (MN985325.1) using Bowtie2 version 2.2.942 with parameters --local --no-mixed -X 1500; PCR duplicates were removed using picard MarkDuplicates, version 2.26.10 (Broad Institute). Digitalized ISH images were automatically analyzed using Visiopharm software v2021.09.02 (Visiopharm, Hørsholm, Denmark). All statistical analysis were performed using SAS version 9.4. The SAS code for statistical analysis has been deposited (https://github.com/niaid/COVID-19-Autopsy-SAS-Code).

For manuscripts utilizing custom algorithms or software that are central to the research but not yet described in published literature, software must be made available to editors and reviewers. We strongly encourage code deposition in a community repository (e.g. GitHub). See the Nature Portfolio guidelines for submitting code & software for further information.

Data

Policy information about availability of data

All manuscripts must include a data availability statement. This statement should provide the following information, where applicable:

- Accession codes, unique identifiers, or web links for publicly available datasets
- A description of any restrictions on data availability
- For clinical datasets or third party data, please ensure that the statement adheres to our policy

The datasets that support the findings of this study are available in Supplementary Data 1, 2 and 3. Positive and negative controls for ISH, IF, and IHC are available in Supplementary Data 3. The sequencing of SARS-CoV-2 isolated from Vero E6-TMPRSS2-T2A-ACE2 cell culture of P38 thalamus has been deposited to GenBank (OP125352).

Field-specific reporting

Please select the one below that is the best fit for your research. If you are not sure, read the appropriate sections before making your selection.

☒ Life sciences ☐ Behavioural & social sciences ☐ Ecological, evolutionary & environmental sciences

For a reference copy of the document with all sections, see nature.com/documents/nr-reporting-summary-flat.pdf

Life sciences study design

All studies must disclose on these points even when the disclosure is negative.

Sample size	The sample size of autopsy cases (n=44) was not predetermined as this was an observational study. Tissue and fluids samples were collected from autopsy each case as able and exact numbers were not predetermined. Cases and tissues selected for sequencing via HT-SGS were determined by gRNA and sgRNA levels within the tissues as determined by ddPCR and qPCR, respectively. n values reported in Extended Data Fig. 4 refer to the depth of sequencing reads recovered for the haplotype(s) detected within the individual tissue.
Data exclusions	No data were excluded from analyses.
Replication	ddPCR results were generated from technical replicates with all samples required to meet manufacturer internal control standard levels. All tissues that underwent ISH, chromogenic IHC, and IF staining had concurrent internal and external positive and negative controls; for ISH images displayed in Fig 2 and Fig. 3 replicates of the listed samples or another sample from the same anatomic location in a different patient were performed; all samples were orthogonally confirmed by ddPCR for SARS-CoV-2 and the ISH assay was validated across a 4-log dynamic range against ddPCR. In Extended Data Fig. 5 all H&E (and Masson trichrome) photomicrographs are exemplars of histopathology observed across a diversity of patients within the cohort, see extended data table 4 and supplemental data 2. The histopathologic observations were validated by a minimum of two board certified anatomic pathologist.
Randomization	This was an observational study.
Blinding	This was an observational study.

Reporting for specific materials, systems and methods

We require information from authors about some types of materials, experimental systems and methods used in many studies. Here, indicate whether each material, system or method listed is relevant to your study. If you are not sure if a list item applies to your research, read the appropriate section before selecting a response.

Materials & experimental systems

n/a	Involved in the study
☐	☒ Antibodies
☐	☒ Eukaryotic cell lines
☒	☐ Palaeontology and archaeology
☒	☐ Animals and other organisms
☒	☐ Human research participants
☒	☐ Clinical data
☒	☐ Dual use research of concern

Methods

n/a	Involved in the study
☒	☐ ChIP-seq
☒	☐ Flow cytometry
☒	☐ MRI-based neuroimaging

Antibodies

Antibodies used	1) Rabbit anti-SARS_CoV_2 Nucleocapsid protein 1 (Wuhan) 1:250, GenScript #U864YFA140-4/CB2093

Antibodies used	2) Mouse anti-NeuN clone A60 1:200, Millipore Sigma #MAB377, lot# 060101159 3) Donkey anti-Rabbit IgG (H+L) Highly cross-Adsorbed Secondary Antibody, Alexa Fluor 488 conjugate, ThermoFisher #A-21206, lot# 2289872 4) Donkey anti-Mouse IgG (H+L) Highly cross-Adsorbed Secondary Antibody, Alexa Fluor 594 conjugate, ThermoFisher #A-21203, lot# 10608644 5) Human TMEM119 Antibody, R&D Systems #MAB10313, lot#CNBT0120051 6) Rabbit IgG, Control Antibody, Vector Laboratories, Inc. #I-1000-5, lot#ZH1201
Validation	1) Validation by Munster et al. described here: https://doi.org/10.1038/s41586-020-2324-7. Antibody was additionally validated by C. Winkler using mock and SARS-CoV-2 infected Vero cells and human cerebral organoids. 2) Validation details can be found here: https://www.emdmillipore.com/US/en/product/Anti-NeuN-Antibody-clone-A60,MM_NF-MAB377, specificity: MILLIPORE's exclusive monoclonal antibody to vertebrate neuron-specific nuclear protein called NeuN (or Neuronal Nuclei) reacts with most neuronal cell types throughout the nervous system of mice including cerebellum, cerebral cortex, hippocampus, thalamus, spinal cord and neurons in the peripheral nervous system including dorsal root ganglia, sympathetic chain ganglia and enteric ganglia. Developmentally, immunoreactivity is first observed shortly after neurons have become postmitotic, no staining has been observed in proliferative zones. The immunohistochemical staining is primarily localized in the nucleus of the neurons with lighter staining in the cytoplasm. The few cell types not reactive with MAB377 include Purkinje, mitral and photoreceptor cells. The antibody is an excellent marker for neurons in primary cultures and in retinoic acid-stimulated P19 cells. It is also useful for identifying neurons in transplants." 3) Details from Thermo Fisher can be found here: https://www.thermofisher.com/antibody/product/Donkey-anti-Rabbit-IgG-H-L-Highly-Cross-Adsorbed-Secondary-Antibody-Polyclonal/A-21206 4) Details from Thermo Fisher can be found here: https://www.thermofisher.com/antibody/product/Donkey-anti-Mouse-IgG-H-L-Highly-Cross-Adsorbed-Secondary-Antibody-Polyclonal/A-21203, validation: These donkey anti-mouse IgG (H+L) whole secondary antibodies have been affinity-purified and show minimum cross-reactivity to bovine, chicken, goat, guinea pig, hamster, horse, human, rabbit, rat, and sheep serum proteins. Cross-adsorption or pre-adsorption is a purification step to increase specificity of the antibody resulting in higher sensitivity and less background staining. The secondary antibody solution is passed through a column matrix containing immobilized serum proteins from potentially cross-reactive species. Only the nonspecific-binding secondary antibodies are captured in the column, and the highly specific secondaries flow through. The benefits of this extra step are apparent in multiplexing/multicolor-staining experiments (e.g., flow cytometry) where there is potential cross-reactivity with other primary antibodies or in tissue/cell fluorescent staining experiments where there may be the presence of endogenous immunoglobulins. 5) Details from R&D Systems can be found here: https://www.rndsystems.com/products/human-tmem119-antibody-1023426_mab10313. 6) Details from Vector Laboratories, Inc. can be found here: https://vectorlabs.com/products/antibodies/rabbit-igg#product.info.overview.

Eukaryotic cell lines

Policy information about cell lines

Cell line source(s)	Vero E6 cells (organism: Cercopithecus aethiops/tissue: kidney/disease: none) were obtained from Ralph Baric at the University of North Carolina, Chapel Hill and Vero E6-TMPRSS2-T2A-ACE2 cells (organism: Cercopithecus aethiops/tissue: kidney/disease: none) were newly procured from BEI Resources (NR-54970; https://www.beiresources.org/Catalog/cellBanks/NR-54970.aspx).
Authentication	Vero E6 cells and Vero E6-TMPRSS2-T2A-ACE2 cells not authenticated in house.
Mycoplasma contamination	All cells are tested monthly to confirm the absence of Mycoplasma.
Commonly misidentified lines (See ICLAC register)	No commonly misidentified cells were used.